AstroDot -a new method for studying the spatial distribution of mRNA in astrocytes

Marc Oudart, Romain Tortuyaux, Philippe Mailly, Noémie Mazaré, Anne-Cécile Boulay, Martine Cohen-Salmon

© 2020. Published by The Company of Biologists Ltd | Journal of Cell Science (2020) 133, jcs239756. doi:10.1242/jcs.239756

TOOLS AND RESOURCES

AstroDot – a new method for studying the spatial distribution of mRNA in astrocytes

Marc Oudart[1,2,*], Romain Tortuyaux[1,2,*], Philippe Mailly[2,3,*], Noémie Mazaré[1,2], Anne-Cécile Boulay[1,2] and Martine Cohen-Salmon[1,2,‡]

ABSTRACT

Astrocytes are morphologically complex and use local translation to regulate distal functions. To study the distribution of mRNA in astrocytes, we combined mRNA detection via *in situ* hybridization with immunostaining of the astrocyte-specific intermediate filament glial fibrillary acidic protein (GFAP). mRNAs at the level of GFAP-immunolabelled astrocyte somata, and large and fine processes were analysed using AstroDot, an ImageJ plug-in and the R package AstroStat. Taking the characterization of mRNAs encoding GFAP-α and GFAP-δ isoforms as a proof of concept, we showed that they mainly localized on GFAP processes. In the APPswe/PS1dE9 mouse model of Alzheimer's disease, the density and distribution of both α and δ forms of *Gfap* mRNA changed as a function of the region of the hippocampus and the astrocyte's proximity to amyloid plaques. To validate our method, we confirmed that the ubiquitous *Rpl4* (large subunit ribosomal protein 4) mRNA was present in astrocyte processes as well as in microglia processes immunolabelled for ionized calcium binding adaptor molecule 1 (Iba1; also known as IAF1). In summary, this novel set of tools allows the characterization of mRNA distribution in astrocytes and microglia in physiological or pathological settings.

KEY WORDS: Astrocytes, Microglia, Hippocampus, mRNA, *In situ* hybridization, Immunofluorescence, ImageJ, APPswe/PS1dE9 mouse, Alzheimer's disease, GFAP

INTRODUCTION

Astrocytes are the most abundant glial cells in the brain. Although astrocyte characteristics vary from one region of the brain to another, they all have a large number of processes that ramify into branches and then secondary branchlets. Hence, protoplasmic astrocytes are large, bushy-shaped cells with diameters of ∼40–60 µm and volumes of ∼10^4 µm^3. Each astrocyte covers a unique domain, and (in humans) contacts up to 2 million synapses (Ogata and Kosaka, 2002). At the synaptic interface, perisynaptic astrocyte processes (PAPs) sense the extracellular interstitial fluid, take up neurotransmitters and ions (Dallérac et al., 2018), and release neuroactive factors (Chever et al., 2014; Sultan et al., 2015). Astrocytes are also in contact with blood vessels; indeed, the latter are entirely sheathed in perivascular astrocyte processes (PvAPs) (Mathiisen et al., 2010). The astrocytes at this interface modulate the integrity and functions of the blood–brain barrier, neuroinflammation (Alvarez et al., 2013; Boulay et al., 2016), cerebral blood flow (Iadecola, 2017) and interstitial fluid drainage (Aspelund et al., 2015). The mechanisms underlying the synaptic and vascular influence of astrocytes are critically important, and have attracted much research interest. Indeed, dysregulation of astrocyte functions and their interplay with neurons and the vascular system contributes to the development and progression of most neurological diseases (Dossi et al., 2018; Iadecola, 2017; Verkhratsky et al., 2015).

Recent studies of astrocyte functional polarity have suggested that mRNA distribution and local translation regulates protein delivery in space and time. In a previous study, we showed that local translation is determined in PvAPs and we characterized the locally translated molecular repertoire (Boulay et al., 2017). Local translation has also been observed in the radial glia during brain development (Pilaz et al., 2016) and in PAPs in the adult cortex (Sakers et al., 2017). Interestingly, these studies showed that some mRNAs were specifically present in low or high levels in the astrocyte soma or processes; hence, mRNA distribution appears to follow specific rules and meet specific needs, and may help to regulate distal perivascular and perisynaptic functions.

To further characterize the mRNA distribution in astrocytes, we developed a new three-dimensional *in situ* method for identifying astrocyte mRNAs localized at the level of GFAP-immunolabelled processes and quantifying them with dedicated bioinformatics tools. More precisely, we studied the distribution of mRNAs encoding the astrocyte-specific GFAP-α and GFAP-δ isoforms (generated by alternative splicing) in the CA1 and CA3 regions of the hippocampus in wild-type (WT) mice and in the APPswe/PS1dE9 mouse model of Alzheimer's disease (AD). We further showed that our approach can be applied to microglia immunolabelled for ionized calcium binding adaptor molecule 1 (Iba1; also known as IAF1) and to all types of mRNA.

RESULTS

Gfapα and *Gfapδ* mRNAs are distributed in PAPs

Gfap mRNAs have been detected in distal perivascular (Boulay et al., 2017) and perisynaptic processes (Sakers et al., 2017) of astrocytes suggesting that local GFAP translation regulates distal intermediate filament assembly. Although previous research focused on the canonical isoform GFAP-α, at least 10 GFAP isoforms (generated by alterative mRNA splicing and polyadenylation signal selection) have been described (Hol and Pekny, 2015; Kamphuis et al., 2012; Middeldorp and Hol, 2011;

[1]Physiology and Physiopathology of the Gliovascular Unit Research Group, Center for Interdisciplinary Research in Biology (CIRB), College de France, CNRS Unité Mixte de Recherche 724, INSERM Unité 1050, Labex Memolife, PSL Research University, Paris 75005, France. [2]Center for Interdisciplinary Research in Biology (CIRB), College de France, Unité Mixte de Recherche 7241 CNRS, Unité1050 INSERM, PSL Research University, Paris 75005, France. [3]Orion Imaging Facility, Center for Interdisciplinary Research in Biology (CIRB), College de France, CNRS Unité Mixte de Recherche 724, INSERM Unité 1050, Labex Memolife, PSL Research University, Paris 75005, France.
*These authors contributed equally to this work

‡Author for correspondence (martine.cohen-salmon@college-de-france.fr)

R.T., 0000-0002-4182-6023; N.M., 0000-0003-4073-8811; A.-C.B., 0000-0001-5620-6209; M.C.-S., 0000-0002-5312-8476

Received 27 September 2019; Accepted 9 February 2020

Journal of Cell Science (2020) 133, jcs239756. doi:10.1242/jcs.239756

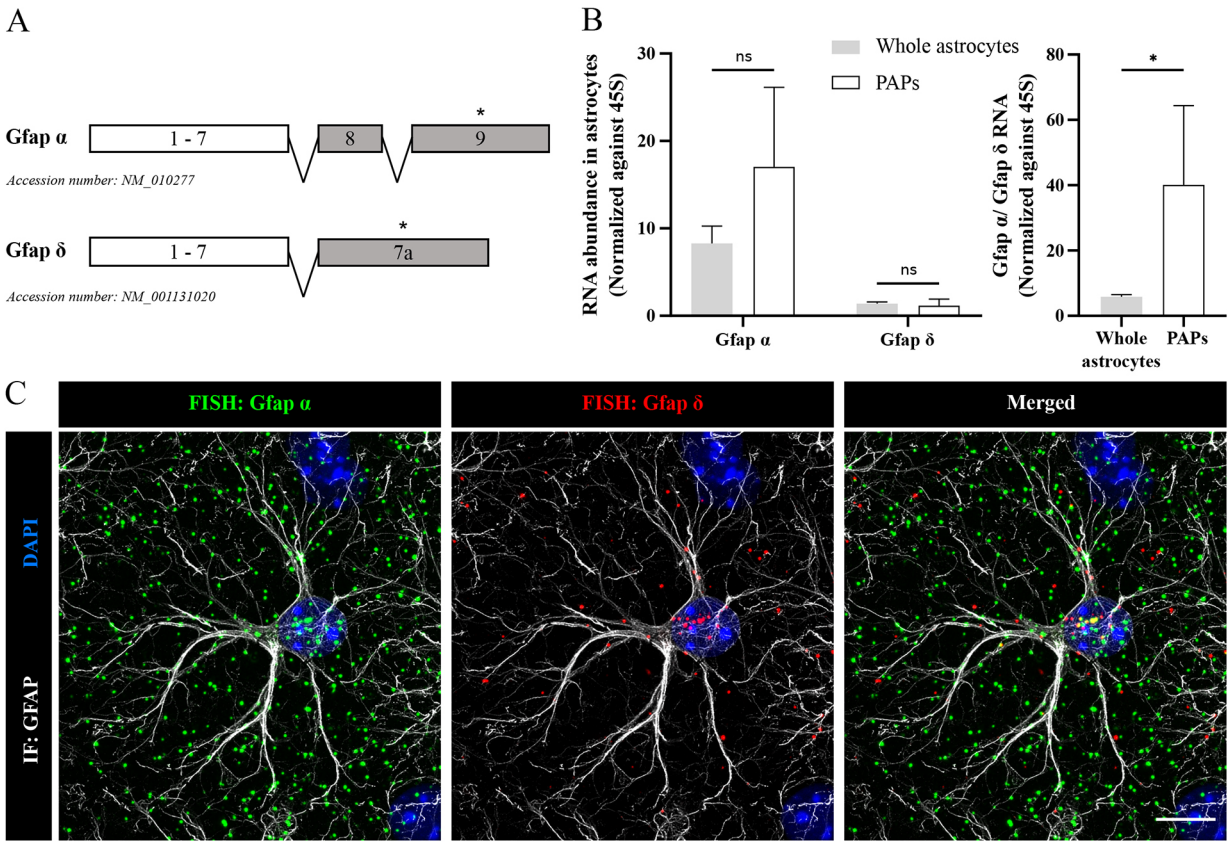

Fig. 1. Detection of *Gfapα* and *Gfapδ* mRNAs in hippocampal astrocytes. (A) Schematic representation of mouse GFAP-α and GFAP-δ isoforms. The positions of the qPCR and FISH probes are indicated with an asterisk. (B) Polysomal *Gfapα* and *Gfapδ* mRNA levels in hippocampal astrocytes and perisynaptic astrocyte processes (PAPs), determined by qPCR and normalized against 45S RNA. Statistical significance was determined in a one-way unpaired Mann–Whitney test; n=3; *P<0.05; ns, not significant. Error bars represent s.e.m. (C) Merged and separated images of a deconvoluted confocal z-stack of a CA1 astrocyte, with FISH detection of *Gfapα* (in green) and *Gfapδ* (in red) mRNAs and co-immunofluorescence detection (IF) of GFAP (in grey). The nucleus was stained with DAPI (in blue). Note the abundance of *Gfapα* mRNA FISH dots (relative to *Gfapδ*) in distal areas of the astrocyte. Scale bar: 10 µm.

Moeton et al., 2016). GFAP-δ is encoded by the same first 7 exons as GFAP-α but has a different C-terminus (Fig. 1A). This isoform has received special interest because it is associated with neurogenic niches (van den Berge et al., 2010) and is expressed in glioma. The GFAP-δ/GFAP-α ratio correlates with the malignancy grade (Brehar et al., 2015; Choi et al., 2009; Heo et al., 2012). In fact, GFAP-δ does not form intermediate filaments alone but integrates the intermediate filament network only if GFAP-α and/or vimentin are present and aggregates or collapses the network when highly expressed in cells (Moeton et al., 2016; Perng et al., 2008). Here, we first looked for *Gfapα* and *Gfapδ* mRNAs in PAPs. Polysomal mRNAs were extracted by translating ribosome affinity purification (TRAP) from adult Aldh1L1:l10a-eGFP mice, which express the chimeric ribosomal protein Rpl10a-eGFP specifically in astrocytes (Heiman et al., 2014). Extractions were performed either from hippocampus (for whole-astrocyte polysomal mRNAs) or synaptogliosome preparations (consisting of apposed pre- and post-synaptic membranes and astrocyte PAPs), in order to extract polysomal mRNAs contained in PAPs (Carney et al., 2014; Sakers et al., 2017). Quantitative qPCR amplification of *Gfapα* and *Gfapδ* mRNA was performed using specific primers (Fig. 1B). Both isoforms were detected in whole astrocytes (mean±s.e.m.: 8.28±1.99 arbitrary units for *Gfapα* and 1.38±0.20 for *Gfapδ*) and in the perisynaptic processes (17.04±9.09 for *Gfapα* and 1.16±0.76 for *Gfapδ*). For polysomal mRNAs, the *Gfapα*/*Gfapδ* ratio was significantly higher in PAPs (40.09±24.27; n=3; P=0.05) than in whole astrocytes (5.81±0.67), suggesting the predominance of Gfapα in PAPs (Fig. 1B).

We next sought to visualize *Gfapα* and *Gfapδ* mRNAs in hippocampal astrocytes. Fluorescent *in situ* hybridization (FISH) was performed on 30-µm-thick free-floating adult mouse brain sections, using specific fluorophore-coupled RNAscope® probes against *Gfapα* exon 9 and *Gfapδ* exon 7a (Fig. 1C). Next, the astrocyte somata and processes were labelled by GFAP immunostaining (Fig. 1C). Importantly, the co-immunofluorescence detection of proteins depends on the preservation of their epitopes during the protease digestion step preceding FISH. We observed dense, continuous, GFAP-labelled arborizations indistinguishable from GFAP immunolabelling obtained without protease treatment (Fig. S1), which indicated that our protocol preserved the GFAP epitopes. In line with the qPCR results presented above, *Gfapα* and *Gfapδ* mRNA FISH signals were detected as discrete dots in the soma and in distal astrocyte areas; *Gfapα* mRNA (Fig. 1B) was more abundant than *Gfapδ*, which was mainly present in the somata (Fig. 1C).

AstroDot and AstroStat: bioinformatics tools for analyzing the mRNA distribution in astrocytes

In order to analyse the distribution of *Gfapα* and *Gfapδ* mRNAs in astrocytes, we developed AstroDot, a dedicated ImageJ plug-in. We had two main objectives: (i) to detect mRNA FISH dots that localized on GFAP-immunostained astrocyte processes; and (ii) to quantify these dots and analyse their distribution in the astrocytes.

Journal of Cell Science (2020) 133, jcs239756. doi:10.1242/jcs.239756

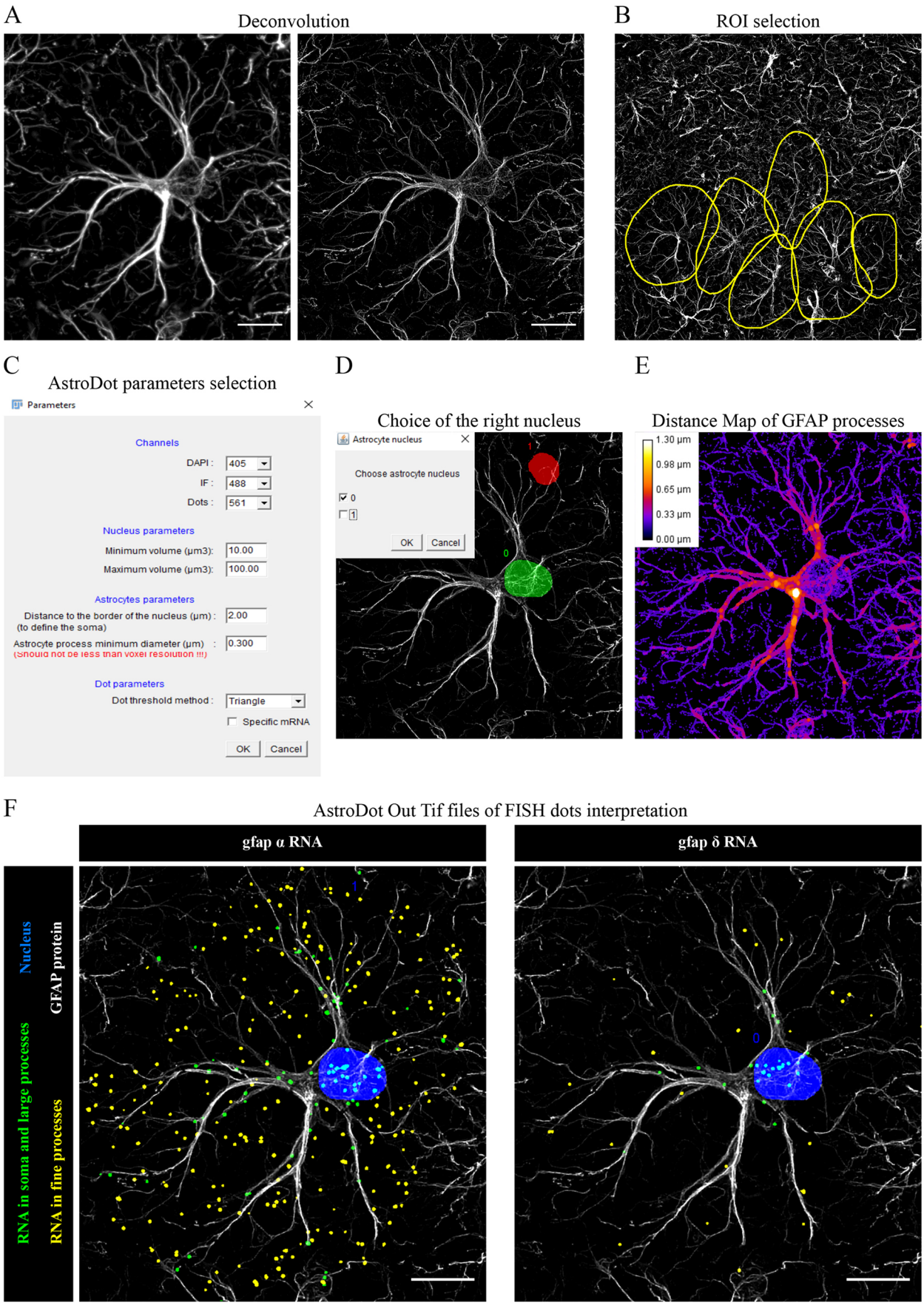

Fig. 2. See next page for legend.

Journal of Cell Science (2020) 133, jcs239756. doi:10.1242/jcs.239756

Fig. 2. AstroDot image processing. All images correspond to a single confocal *z*-stack for a CA1 astrocyte. (A) Effect of deconvolution on GFAP immunofluorescence. Left panel: raw confocal image; right panel: deconvoluted images. (B) Selection of regions of interest (ROIs; yellow circles). (C) AstroDot dialogue box for the definition of fluorescence channels, the nucleus and astrocyte parameters, the threshold method for FISH dots and the choice of the 'Specific mRNA' option. (D) Detection of the astrocyte nucleus (in green) and other nuclei (in red). (E) Heat map of GFAP immunofluorescence, used to calculate the process diameter. (F) AstroDot interpretation of the results for *Gfapα* and *Gfapδ* mRNAs, with the 'Specific mRNA' option active. Green dots are located in the soma or large GFAP-labelled processes. Yellow dots are located in fine processes. Scale bars: 10 µm.

Confocal images of the CA1 and CA3 regions of the hippocampus were acquired and then deconvoluted, so as to eliminate the inherent fluorescence blurring [the point spread function (PSF)] and noise, and to increase the resolution (Fig. 2A). Astrocytes define individual domains, and GFAP processes do not intermingle (Bushong et al., 2002). Using this property, regions of interest (ROIs, i.e. the soma and processes) corresponding to individual astrocytes were selected manually by assessing the GFAP (intermediate filaments) and DAPI (nuclei) staining on the *Z*-projection of image stacks and by defining the stack of confocal planes for each ROI (Fig. 2B). AstroDot opens with a dialogue box (Fig. 2C) that enables the operator to attribute: (1) a specific purpose for each of the three fluorescence channels, e.g. 'DAPI' for nuclear staining, 'IF' for GFAP immunofluorescence, and 'Dots' for FISH dot thresholding and detection; (2) a minimum and maximum nucleus volume; (3) a distance from the DAPI staining to define the somatic domains; (4) a minimum astrocyte process diameter. This value should not be less than the Voxel resolution. This dialogue box also contains a 'Specific mRNA' option, which can be selected when the studied mRNA is expressed only in the cell-type of interest as is the case here for *Gfap* in astrocytes. In such situations, all mRNA FISH dots are considered to belong to this cell type. The first step in the analysis was calculation of the mean GFAP immunofluorescence background, i.e. the value above which the signal was considered to be positive. Importantly, to verify the background homogeneity, this value was calculated on whole images as well as on individual ROIs. In the second step, each astrocyte nucleus was defined; given that astrocytes interact with other brain cell types, some ROIs can contain more than one nucleus. AstroDot was designed to optimize the recognition of astrocyte nuclei on the basis on the GFAP immunostaining. The putative astrocyte nucleus appears in green, and any other nuclei appears red. A second dialogue box allows the operator to confirm or modify AstroDot's automatic selection by clicking on the correct nucleus (Fig. 2D). AstroDot then starts to detect astrocyte mRNAs, based on their localization at the level of the GFAP immunostaining. A distance map is used to calculate the diameter of each GFAP-immunolabelled process. Processes with a diameter greater than the minimum distance between two confocal planes (0.3 µm, in the present case), are defined as 'large', and those with a smaller diameter as 'fine' (Fig. 2E). The DAPI staining and the surrounding 2 µm space corresponded here to the somatic domain of each astrocyte. A TIF image was generated for each ROI (Fig. 2F). The mRNA FISH dots are red if they were outside astrocytes, green if they localize on astrocyte large processes and somata, or yellow if they localize on astrocyte fine processes (Fig. 2F). All the results were automatically entered on a table with the following items for each ROI: (1) image name; (2) ROI name; (3) background intensity; (4) astrocyte volume; (5) dot density in astrocytes; (6) percentage of dots not in astrocytes; (7) percentage of dots in astrocyte somata; (8) percentage of dots in astrocyte fine processes; (9) percentage of dots in astrocyte large processes; (10) mean astrocyte process diameter. To facilitate the statistical analysis of AstroDot data, we developed an optional R package named AstroStat; it automatically calculates and compares the mean±s.d. values, and produces a summary report of the results.

Characterization of *Gfapα* and *Gfapδ* mRNAs in CA1 and CA3 hippocampal astrocytes from WT mice and the APPswe/PS1dE9 mouse model of AD

We analysed the density and distribution of *Gfapα* and *Gfapδ* mRNAs in CA1 and CA3 hippocampal adult astrocytes in WT adult mice by using the AstroDot 'Specific mRNA' option (Fig. 3 and Tables S2–S5). Comparison of the astrocytes in CA1 versus CA3 indicated that CA1 astrocytes had a slightly greater overall volume but displayed processes with the same mean diameter (Fig. 3A). The *Gfapα*/*Gfapδ* mRNA ratio was the same in the two regions (Fig. 3B). Overall, and in line with our initial qPCR analysis (Fig. 1B), *Gfapα* was 5.2 times more abundant than *Gfapδ* in both CA1 and CA3 (Fig. 3C). Both mRNAs were more abundant in the processes (*Gfapα*, 88.5±6.7% in CA1 and 86.7±8.1% in CA3; *Gfapδ*, 73.4±11.3% in CA1 and 71.5±16.4% in CA3; mean±s.d.) than in the soma. *Gfapδ* was more abundant than *Gfapα* in the soma and in large processes (Fig. 3D). We next analysed the data without considering the astrocytic-specific expression of GFAP, unselecting the 'Specific mRNAs' option of AstroDot (Fig. 3E). In this case, both *Gfapα* and *Gfapδ* mRNAs were localized on GFAP-labelled intermediate filaments in CA1 (mean±s.d.: 59.5±9.0 for *Gfapα* and 74.4±11.0 for *Gfapδ*) and CA3 (62.2±10.1 for *Gfapα* and 74.7±12.4 for *Gfapδ*), suggesting that the majority of *Gfap* RNAs are associated with intermediate filaments (Fig. 3E).

Astrocytes are involved in neuroinflammation, and become reactive in virtually all pathological situations in the brain. Astrocyte reactivity is characterized by GFAP overexpression and morphological changes, such as process hypertrophy and remodelling (Hol and Pekny, 2015). Hence, we next sought to study *Gfapα* and *Gfapδ* mRNAs in reactive astrocytes. We chose the example of AD, in which astrocytes undergo drastic morphological and molecular changes that perturb their physiology (Ben Haim et al., 2015; Burda and Sofroniew, 2014). Using the method described above, *Gfapα* and *Gfapδ* mRNA FISH dots were detected on GFAP-immunolabelled sections of CA1 and CA3 hippocampus from 9-month-old APPswe/PS1dE9 mice (Fig. 4). We quantified astrocytes associated with a beta-amyloid plaque (Aβ, labelled with DAPI) or more than 30 µm from an Aβ plaque (Fig. 5 and Tables S2–S5). As reported in the literature, CA1 and CA3 astrocytes from APP/PS1dE9 mice were larger than those from WT mice (Fig. 5A) but had a slightly smaller process diameter (Fig. 5A). In astrocytes not associated with Aβ, the *Gfapα*/*Gfapδ* ratio was slightly but significantly higher (by a factor of 1.3) in CA1 and CA3 (Fig. 5B), with a higher *Gfapα* mRNA level in fine processes only (Figs 4A and 5F). In contrast, the *Gfapδ* mRNA density was the same as in WT mice in CA1 and CA3 (Fig. 5C). However, the distribution of this mRNA within the astrocytes differed; levels in large processes were lower (relative to the WT) in CA1 and CA3 (Fig. 5E), and levels in fine processes were higher in CA3 only (Fig. 5F). The relative differences in mRNA levels were greater in Aβ-associated astrocytes (Fig. 4B); the density of *Gfapα* mRNAs was significantly higher than in WT cells (5.0-fold for CA1, and 4.7-fold in CA3) or in astrocytes not associated with Aβ (3.8-fold for CA1, and 3.7-fold in CA3) (Fig. 5C). The distribution of *Gfapα* mRNA also differed, with lower

Journal of Cell Science (2020) 133, jcs239756. doi:10.1242/jcs.239756

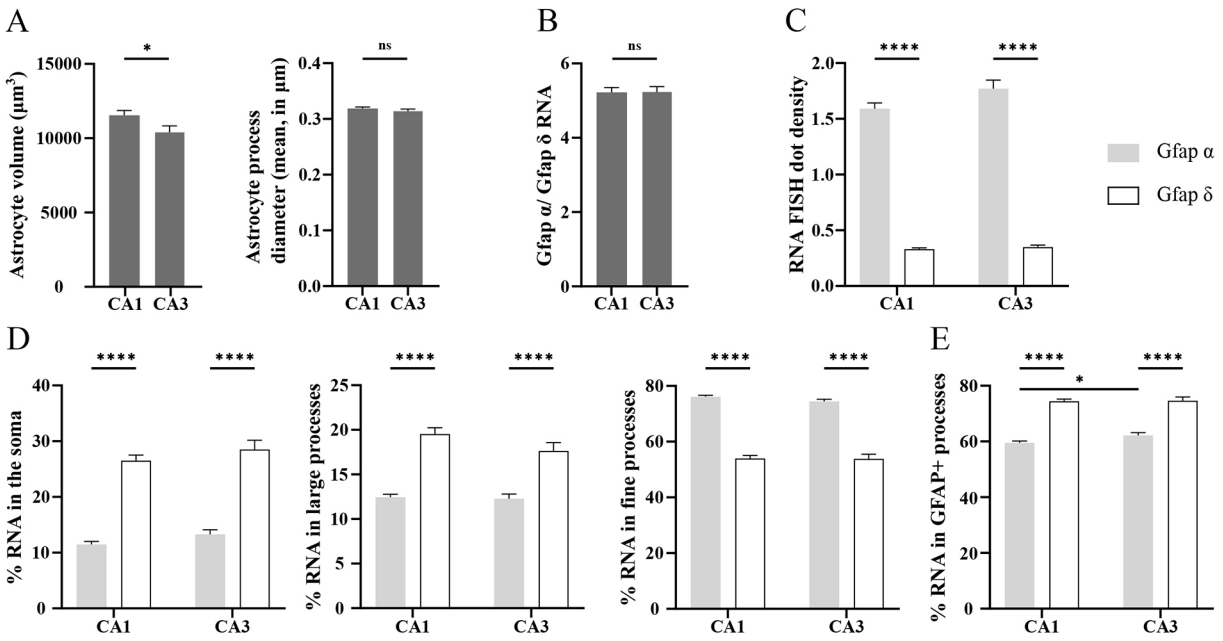

Fig. 3. Distribution of *Gfapα* and *Gfapδ* mRNAs in CA1 and CA3 hippocampal astrocytes. (A) Astrocyte volume, and process diameter. (B) The *Gfapα*/*Gfapδ* mRNA ratio. (C) Total mRNA density: number of RNA FISH dots/µm^3×100. (D) Percentages of *Gfapα* and *Gfapδ* mRNAs in astrocyte somata, fine processes and large processes. (E) Percentages *Gfapα* and *Gfapδ* mRNA dots localized on GFAP when the 'Specific mRNA' option was not applied. In total, 175 CA1 and 94 CA3 astrocytes from 3 mice and 5 slices per mouse were analysed (values are presented in Tables S2–S5). Statistical significance was determined in two-way unpaired Student's *t*-tests. *P<0.05; ****P<0.0001; ns, not significant. Error bars represent the s.e.m.

levels (relative to the WT) in the soma (Fig. 5D) and in large processes (only in CA1) (Fig. 5E) and higher levels in fine processes in CA1 and CA3 (Fig. 5F). The same effect was observed for the *Gfapδ* mRNA, with a greater abundance in Aβ-associated astrocytes than in WT samples (3.6-fold for CA1, and 3.5-fold in CA3) or in astrocytes far from plaques (3.3-fold for CA1, and 3.4-fold in CA3) (Fig. 5C). The redistribution was most prominent in fine processes in CA1 and CA3 (Fig. 5F). These results show that the density and distribution of *Gfapα* and *Gfapδ* mRNAs vary markedly as a function of the astrocyte's reactivity status, the brain area and the proximity of Aβ deposits.

Application of AstroDot and AstroStat to the analysis of ubiquitous mRNAs in astrocytes and microglia

To further validate our approach, we studied the distribution of *Rpl4* mRNA (a ubiquitously expressed mRNA encoding the large subunit ribosomal protein 4) in CA1 (Fig. 6A). Interestingly, 62.52±11.77% of the *Rpl4* mRNA FISH dots were localized in astrocytes (n=67). Of these, 83.33±5.41% were present in fine GFAP-immunolabelled processes, with 9.59±3.45% in large GFAP-immunolabelled processes, and 7.09±4.14% in somata (all values are mean±s.d.). This result was unexpected because Rpl4 integrates into the 60S ribosome subunit in the nucleus (Huber and Hoelz, 2017), but was corroborated by a qPCR analysis (performed as described above) of polysomal mRNAs extracted by TRAP from adult Aldh1L1:l10a-eGFP mouse hippocampus or PAPs; in the latter, Rpl4 was enriched 120-fold (P=0.05, n=3) (Fig. 6B). To study the distribution of non-astrocyte *Rpl4* mRNA FISH dots, we performed additional, independent experiments by immunostaining neuronal and microglial specific markers. Immunostaining of the neuronal-specific cytoskeletal high and medium chains of the neurofilament protein (NF-H and NF-M), the microtubule-associated protein 2 (MAP2) and the hippocampal immature neuron protein doublecortin (DCX) was however not preserved enough even after a mild FISH protease pre-treatment (Fig. S2). In contrast, as with the GFAP immunofluorescence experiments, our FISH protocol was compatible with the detection of the microglial-specific Iba1 protein, which was detected and remained homogeneous throughout the somata and processes (Fig. 6C). Our analysis of the distribution of *Rpl4* mRNA in microglia (n=28) indicated that 16.07±4.47% of the *Rpl4* mRNA FISH dots were localized in microglial processes. Of these, 37.72±9.24% were localized in fine processes, with 27.06±10.78% in large processes and 35.22±10.13% in somata (means±s.d.). In conclusion, this novel set of tools allows the characterization of mRNA distribution in astrocytes and microglia.

DISCUSSION

Although local translation has been recently described in astrocyte processes, tools for studying the distribution of astrocyte mRNAs were not previously available. Accordingly, we developed a co-labelling method that combined mRNA *in situ* hybridization, the immunofluorescence detection of GFAP-containing intermediate filaments on brain slices, confocal imaging and a bioinformatics analysis of mRNA density and distribution in astrocytes.

A key technical obstacle to the implementation of this approach was the risk of protein epitope degradation during the protease digestion step that precedes *in situ* RNA hybridization. Our previous tests on transgenic hGfap-eGFP mouse brain sections (in which eGFP fills the astrocyte cytoplasm; Nolte et al., 2001) indicated that these adaptations were not sufficient to preserve eGFP (data not shown) and thus precluded the use of this reporter mouse strain to detect astrocytes in parallel with *in situ* hybridization. In contrast to previous reports (Boulay et al., 2017; Pilaz et al., 2016), however, our protocol preserved GFAP and enabled us to perform parallel *in situ* hybridization and GFAP immunodetection. Interestingly, these conditions also allowed us to immunodetect the microglia-specific

Journal of Cell Science (2020) 133, jcs239756. doi:10.1242/jcs.239756

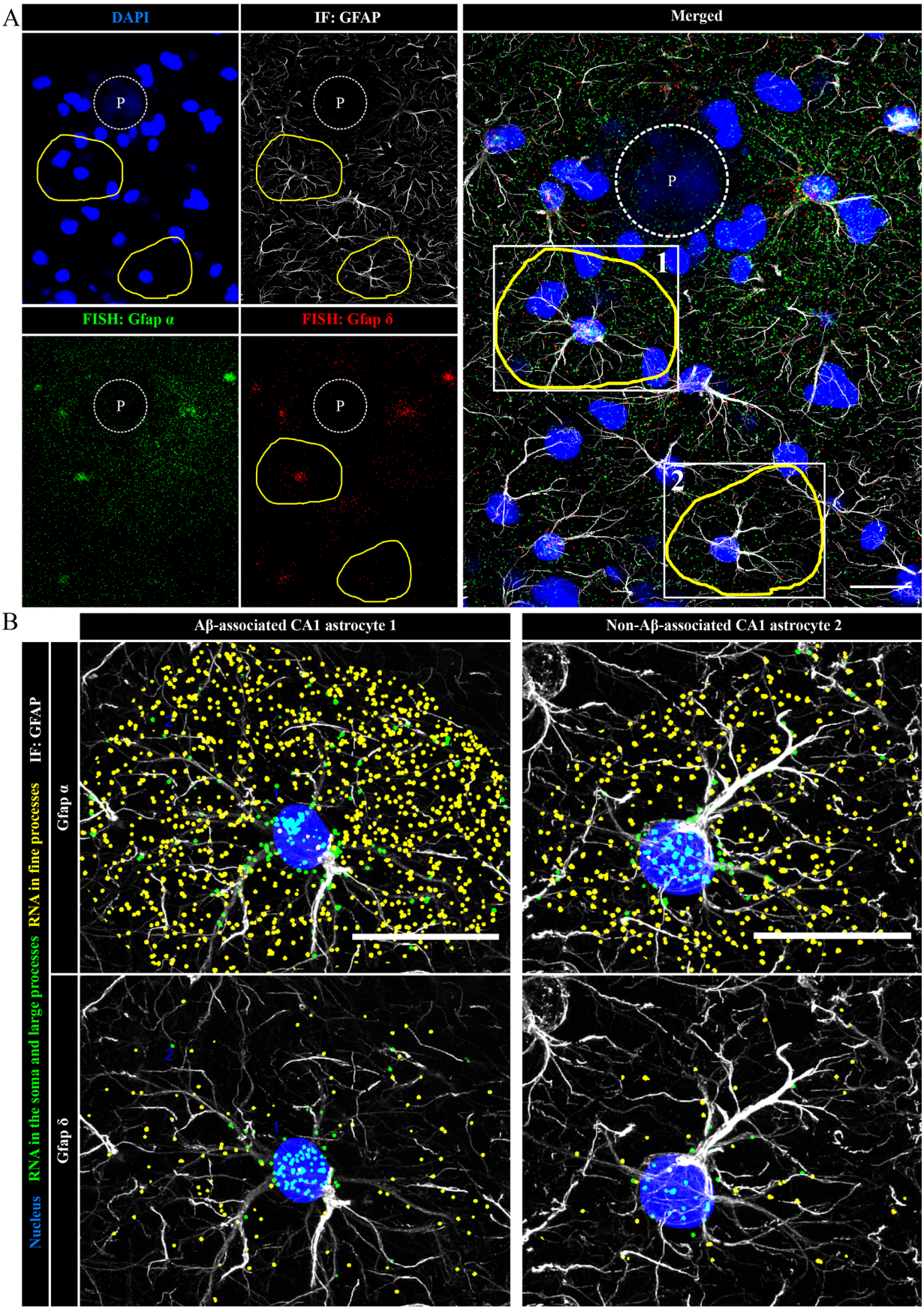

Fig. 4. See next page for legend.

Journal of Cell Science (2020) 133, jcs239756. doi:10.1242/jcs.239756

Fig. 4. Detection of *Gfapα* and *Gfapδ* mRNAs in CA1 hippocampal APPswe/PS1dE9 astrocytes. (A) Merged and separated images of a deconvoluted confocal *z*-stack of APPswe/PS1dE9 CA1 astrocytes, with FISH detection of *Gfapα* mRNA (in green) and *Gfapδ* mRNA (in red) and co-immunofluorescence detection of GFAP (in grey). The nucleus and an amyloid deposit (dotted circle labelled 'P') are stained with DAPI (in blue). ROI #1 (yellow circle) is an astrocyte close to an Aβ deposit. ROI #2 is located more than 60 µm from an Aβ plaque. (B) TIF images of ROI1 and ROI2 for *Gfapα* and *Gfapδ* mRNA, as analysed with AstroDot using the 'Specific mRNA' option. Green dots belong to the soma and large GFAP-labelled immunofluorescent processes. Yellow dots belong to fine processes. Scale bars: 20 µm.

Iba1. In contrast to glial cells, we could not find any neuronal immunolabelling preserved after the FISH pre-treatment. Further efforts are therefore needed to eventually find compatible markers.

It is noteworthy that GFAP is not expressed uniformly in the brain, and so GFAP immunolabelling is somewhat limited by its lack of applicability to all brain regions. Nevertheless, our optimization of the GFAP immunolabelling makes it possible to distinguish between labelled astrocyte processes and their secondary extensions in regions where GFAP is highly expressed (e.g. the hippocampus, olfactory bulbs, cerebellum and hypothalamus). Another advantage of immunolabelling GFAP and Iba1 relates to the fact that both proteins are standard markers of glial reactivity – a process initiated in response to immune attack, chronic neurodegenerative disease or acute trauma (Liddelow and Barres, 2017). Hence, GFAP and Iba1 co-immunolabelling could therefore be used to address possible changes in mRNA distribution in reactive astrocytes and microglia, as demonstrated here in APPswe/PS1dE9 mice.

It was previously determined that GFAP immunolabelling delineates only 15% of the total astrocyte volume (Bushong et al., 2002). Nevertheless, we found that the majority of the *Gfapα* and *Gfapδ* mRNA dots were attributed to GFAP processes. The mRNA dots not detected in GFAP intermediate filaments probably belonged to fine distal astrocyte processes where GFAP is less present (e.g. PAPs). These observations suggest that the majority of *Gfap* mRNAs are bound to intermediate filaments, and are consistent with previous reports of colocalization between mRNAs encoding collagens (Challa and Stefanovic, 2011) and alkaline phosphatase (Schmidt et al., 2015) on one hand and vimentin (another intermediate filament protein) on the other. Taken as a whole, these findings suggest that intermediate filaments may have crucial roles in the distal distribution of mRNAs. Consequently, it is conceivable that GFAP alterations, deficiency or upregulation (one or the other of which occurs in most neuropathological conditions; Hol and Pekny, 2015) might greatly modify the distribution of astrocyte mRNAs and their local translation. In turn, these changes might alter the astrocyte functions, particularly at their synaptic and vascular interfaces.

In order to demonstrate the applicability of our approach, we first focused on mRNAs encoding (i) the canonical α isoform of GFAP and (ii) the δ Cter variant, the assembly of which with GFAP-α promotes intermediate filament aggregation and dynamic changes (Moeton et al., 2016; Perng et al., 2008). Interestingly, the results of our experiments in WT mice showed that *Gfapδ* mRNA was more likely than *Gfapα* mRNA to be found in the astrocyte soma. This finding corroborated the results of a previous *in vitro* study in which the proportion of mRNA in primary astrocyte protrusions was higher

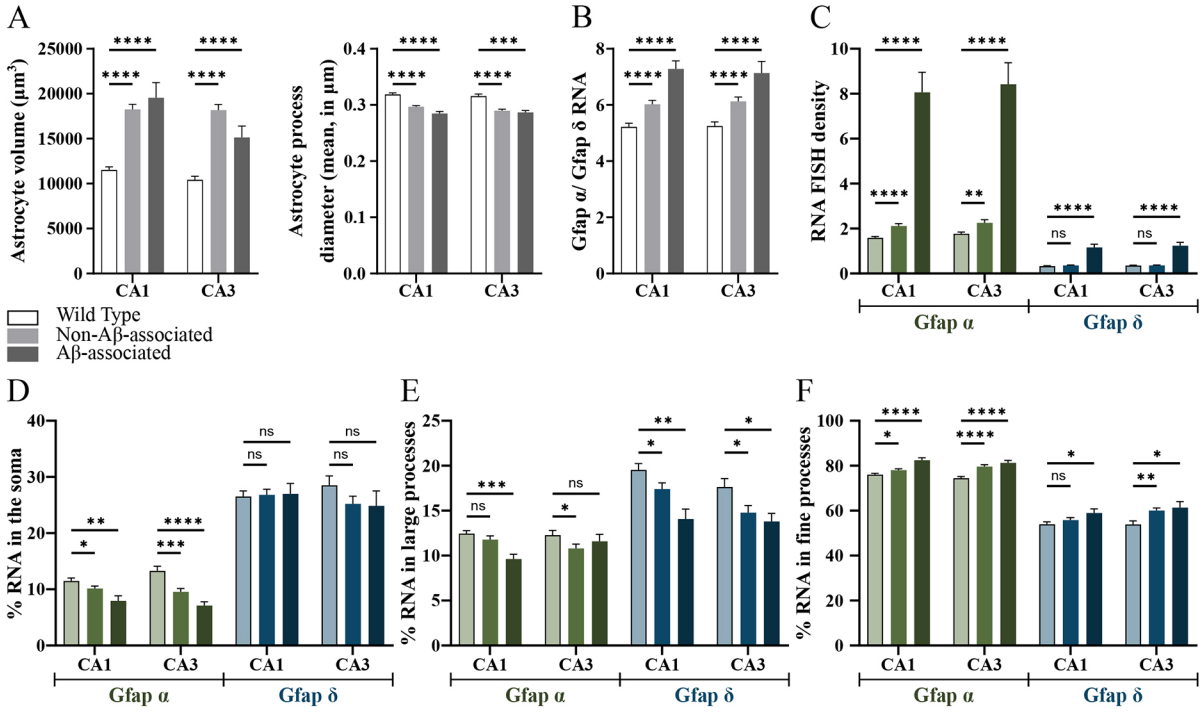

Fig. 5. Comparison of *Gfapα* and *Gfapδ* mRNA densities and distributions in CA1 and CA3 hippocampal astrocytes from WT and APPswe/PS1dE9 mice. (A) Astrocyte volume and process diameter. (B) The *Gfapα*/*Gfapδ* mRNA ratio. (C) Total mRNA density: number of RNA FISH dots/µm^3×100. (D-F) Percentages of *Gfapα* and *Gfapδ* mRNA dots localized on GFAP immunostaining in astrocyte somata (D), fine processes (E) and large processes (F). Analyses were performed on 175 CA1 WT astrocytes, 94 CA3 WT astrocytes, 127 APPswe/PS1dE9 CA1 astrocytes not associated with plaques, 78 APPswe/PS1dE9 CA3 astrocytes not associated with plaques, 27 plaque-associated CA1 APPswe/PS1dE9 astrocytes, and 28 plaque-associated CA3 APPswe/PS1dE9 astrocytes. 3 mice per genotype and 5 slices per mouse were analysed (values are presented in Tables S2–S5). Statistical significance was determined using two-way unpaired Student's *t*-tests. **P*<0.05; ***P*<0.001; ****P*<0.001; *****P*<0.0001; ns: not significant. Error bars represent s.e.m.

Journal of Cell Science (2020) 133, jcs239756. doi:10.1242/jcs.239756

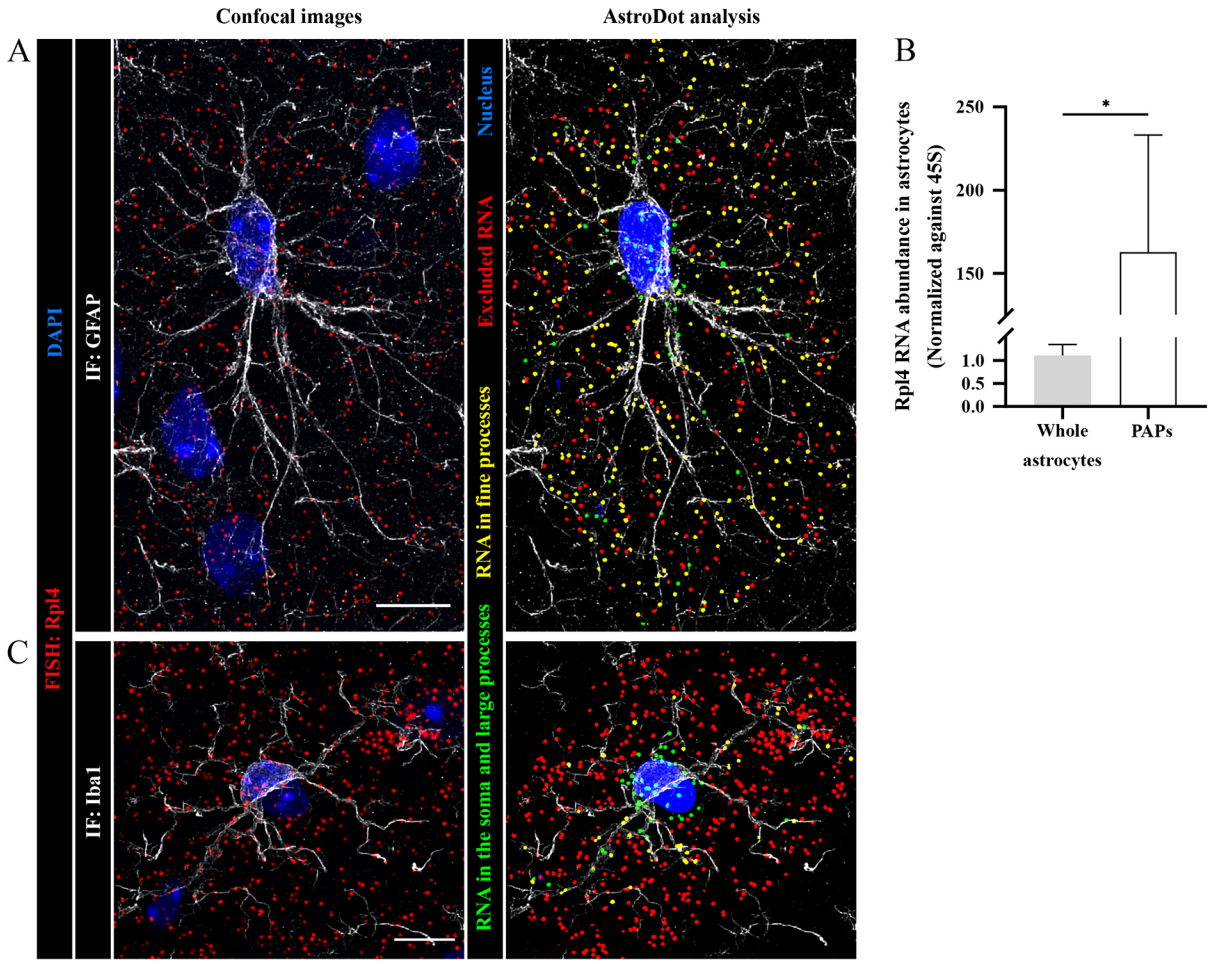

Fig. 6. Detection and characterization of *Rpl4* mRNA distribution in CA1 hippocampal astrocytes, microglia. (A) Left: Confocal *z*-stack of a CA1 astrocyte with FISH detection of *Rpl4* mRNA (in red) and co-immunofluorescence GFAP detection (in grey). The nucleus is stained with DAPI (in blue). Right: AstroDot analysis. Green dots are located in the soma or in GFAP-immunolabelled large processes; yellow dots are located in GFAP-immunolabelled fine processes; red dots are not localized on GFAP immunostaining (i.e. excluded RNAs). (B) The polysomal *Rpl4* RNA level in hippocampal astrocytes and PAPs, determined by qPCR and normalized against 45S RNA. Statistical significance was determined in a one-way unpaired Mann–Whitney's test; $n=3$; *$P<0.05$. Error bars represent s.e.m. (C) Left: confocal *z*-stack of a CA1 microglial cell with FISH detection of *Rpl4* mRNA (in red) and co-immunofluorescent Iba1 (in grey). The nucleus was stained with DAPI (in blue). Right: AstroDot analysis. Green dots are located in the soma or Iba1-immunolabelled large processes; yellow dots are located in Iba1-immunolabelled fine processes; red dots do not localize on Iba1 immunostaining (i.e. excluded RNAs). Scale bars: 10 µm.

for *Gfapα* than for *Gfapδ* (Thomsen et al., 2013). The high *Gfapα* and *Gfapδ* mRNA density observed in amyloid plaque-associated astrocytes was also consistent with previous qPCR-based assays of mRNA in the cortex of APPswe/PS1dE9 mice (Kamphuis et al., 2012). Interestingly, levels of human GFAP-α and GFAP-δ isoforms are elevated in plaque-associated astrocytes in the CA1-3 region (Kamphuis et al., 2014). Although RNA density in fine processes could also be secondary to the increase in GFAP filament density linked to astrocyte reactivity, our observations of elevated mRNA density and distribution in the fine processes of plaque-associated astrocytes suggest that local translation of *Gfapα* and *Gfapδ* mRNA might be a critical mechanism for regulating intermediate filament dynamics in distal astrocyte processes during the progression of AD. Given that the GFAP-α/GFAP-δ isoform ratio is known to strongly influence astrocyte proliferation and malignancy (Stassen et al., 2017; van Bodegraven et al., 2019), our approach might constitute a valuable tool for accurately assessing the differentiation state of astrocytomas in preclinical and clinical settings.

Lastly, we demonstrated that our approach is applicable to any type of mRNA and can also be used in microglia. In fact, the present study is the first to have demonstrated that mRNAs are distributed across microglial processes; this is an important observation in view of the microglia's complex morphology and motility, and its roles in immune surveillance and synaptic remodelling in the brain (Squarzoni et al., 2014). Our results strongly suggest that mRNA distribution and local translation are of physiological significance in this important neural cell type. In conclusion, our new semi-automated *in situ* histological method is the first to have characterized mRNA distribution in astrocytes and microglia.

MATERIALS AND METHODS

Mice

Aldh1L1:l10a-eGFP mice (Heiman et al., 2014) and C57BL6 WT mice were housed under pathogen-free conditions in the animal facility at the Centre Interdisciplinaire de Recherche en Biologie (CIRB, Collège de France, Paris, France). The APPswe/PS1dE9 (Borchelt et al., 1997) mice were housed in the MIRCen animal facility (CEA, Fontenay-aux-Roses, France). All analyses were performed on 3 mice (males) per genotype.

Ethical approval

All experiments were approved by the French Ministry of Research and Higher Education, and conducted in accordance with the host institution's ethical standards (Collège de France, Paris, France).

Journal of Cell Science (2020) 133, jcs239756. doi:10.1242/jcs.239756

Aldh1L1:l10a-eGFP TRAP from whole astrocytes and PAPs, and qPCR

Two hippocampi from 5-month-old mice were used for each whole-astrocyte polysome extraction. Each synaptosome preparation was done on four hippocampi as described in Carney et al. (2014) for perisynaptic astrocyte extraction. Polysomes were extracted using the method described in Boulay et al. (2019). Three independent samples were prepared for qPCR analysis. Messenger RNAs were purified using the RNeasy Lipid tissue kit (Qiagen). cDNA was synthesized from 100 ng of whole-astrocyte RNA or PAP mRNA using a Reverse Transcriptase Superscript III kit (Invitrogen) with random primers, and stored at −20°C. Next, 1 µl of cDNA suspension was pre-amplified using SoAmp reagent (Bio-Rad), and droplet qPCR was performed using a QX200™ Droplet Digital™ PCR System (Bio-Rad). The cDNA content was normalized against 45S RNA. TaqMan probes and primer references are listed in Table S1. The data were analysed by applying a one-way unpaired Mann–Whitney test. The threshold for statistical significance was set to $P<0.05$.

Brain slice preparation

Nine-month-old mice were anaesthetized with a mix of ketamine and xylazine (0.1 ml/mg) and killed by transcardiac perfusion with 1× phosphate-buffered saline (PBS) with 4% paraformaldehyde (PFA). The brain was removed and immersed in 4% PFA overnight at 4°C. The PFA solution was replaced with 15% sucrose for 24 h at 4°C and, lastly, by 30% sucrose for 24 h at 4°C. The brains were cut into 30-µm-thick coronal sections using a Leitz microtome (1400). Sections were stored at −20°C in a cryoprotectant solution (30% glycerol and 30% ethylene glycol in 1× PBS).

Fluorescent *in situ* hybridization and immunostaining

Slices were carefully washed three times with 1× PBS in a 24-well plate. For the last wash, the 1× PBS was replaced with 7 drops of RNAscope® hydrogen peroxide solution (Advanced Cell Diagnostics Inc.) for 10 min at room temperature (RT); this blocked endogenous peroxidase activity, and resulted in the formation of small bubbles. The slices were washed in Tris-buffered saline with Tween® (50 mM Tris-Cl, pH 7.6; 150 mM NaCl, 0.1% Tween® 20) at RT, and mounted on Super Frost+®-treated glass slides using a paintbrush. Slices were dried at RT for 1 h in the dark, quickly (in less than 3 s) immersed in deionized water in a glass chamber, dried again for 1 h at RT in the dark, incubated for 1 h at 60°C in a dry oven, and dried again at RT overnight in the dark.

The slices were rehydrated by rapid immersion (for less than 3 s) in deionized water at RT. Excess liquid was removed with an absorbent paper, and a hydrophobic barrier was drawn. A drop of pure ethanol was applied on the slice for less than 3 s and removed using an absorbing paper. The slides were incubated at 100°C in a steamer, while ensuring that condensation did not fall back on them. A drop of preheated RNAscope® 1× Target Retrieval Reagent (Advanced Cell Diagnostics Inc.) was added to the steamer, and the slides were left for 15 min. Next, the slides were washed three times in deionized water at RT, and excess liquid was removed with absorbent paper. A drop of 100% ethanol was applied for 3 min, and excess liquid was then removed. A drop of RNAscope® Protease+ solution (Advanced Cell Diagnostics Inc.) was applied and slices were incubated at 40°C in a humid box for 30 min. Target retrieval treatment and RNAscope® Protease+ treatment were used to unmask the mRNAs. Lastly, the slides were washed three times with deionized water at RT. For neuronal assays (Fig. S2), several pre-treatment conditions were tested: no protease, Protease 3, Protease 4 and Protease+ of the RNAscope® Multiplex Fluorescent Reagent Kit v2 (Advanced Cell Diagnostics Inc.) during 10, 20, or 30 min.

FISH was performed using the RNAscope® Multiplex Fluorescent Reagent Kit v2 (Advanced Cell Diagnostics Inc.) and specific probes (Table S1; Fig. S3), according to the manufacturer's instructions. Following the FISH procedure, slides were incubated with a blocking solution (0.2% normal goat serum, 0.375% Triton X-100 and 1 mg ml^{-1} bovine serum albumin in 1× PBS) for 1 h at RT, incubated with the primary antibody overnight at 4°C (Table S1), rinsed three times with 1× PBS, and incubated with the secondary antibody (Table S1) for 2 h at RT. Lastly, the slides were washed three times in 1× PBS and mounted in Fluoromount-G® and DAPI (Southern Biotech).

Imaging

Images were acquired using a Yokogawa W1 Spinning Disk confocal microscope (Zeiss) with a 63× oil objective (1.4 numerical aperture). The imaging conditions and acquisition parameters were the same for all slides. The experimental PSF was obtained using carboxylate microsphere beads (diameter: 170 nm; Invitrogen/ThermoFisher Corp.). Except for DAPI, all channels were deconvoluted with Huygens Essential software (version 19.04, Scientific Volume Imaging, The Netherlands; http://svi.nl), using the classic maximum likelihood estimation algorithm and a signal-to-noise ratio of 50 (for the immunofluorescence channel) or 20 (for the FISH channel), a quality change threshold of 0.01, and 150 iterations at most.

AstroDot and AstroStat

As shown in the Results section, AstroDot can be used to study mRNA density and distribution not only in astrocytes but also in microglia immunolabelled for Iba1. In addition to FISH signals, AstroDot can be used to quantify any type of dot-shaped fluorescence signal. AstroStat was used to analyse the AstroDot results table, using an R script. The programs can be downloaded free of charge from https://github.com/pmailly/Astrocyte_RNA_Analyze and https://github.com/rtortuyaux/astroStat, respectively.

For AstroDot, an image analysis plug-in was developed for the ImageJ/Fiji software (Schindelin et al., 2012; Schneider et al., 2012), using Bio-Format (openmicroscopy.org), mcib3D (Ollion et al., 2013), GDSC (https://github.com) and local thickness (https://imagej.net/Local_Thickness) libraries.

ROIs enclosing each astrocyte were drawn by hand, using the Fiji polygon tool on the *Z*-projection of the stack, and using the ImageJ option 'Max intensity'. In the ROI Manager, the ROI names were coded as (roi_number-z_top-z_bottom) and saved in a zip file.

AstroDot processing

The plug-in was designed to process all images in a specific folder containing MetaMorph .nd files, and to read metadata images (channel name, z step, etc.), deconvoluted image channels (except for DAPI), and ROI zip files. Steps followed were as below:

1. AstroDot's parameters (the image folder, the channel order, the threshold method, etc.) were displayed in a dialogue box (see Fig. 2C).
2. The immunofluorescence background was estimated on whole images using a 0.5 median filter, a binary mask (using Li's threshold method), and an inversion of the binary mask (Li and Lee, 1993; Li and Tam, 1998). The immunofluorescence value was multiplied by the inverted mask and then divided by 255. The background value (bgThreshold) was defined as the mean intensity of all voxels other than those with a value of zero. To ascertain the background homogeneity, we also recommend this calculation is performed on individual ROIs to check that values are comparable.
3. For each ROI, a substack corresponding to zTop and zBottom (defined in the ROI name) was created for all channels.
4. For semi-automatic determination of the astrocyte or microglial cell nucleus, DAPI fluorescence was processed by removing DAPI potential background with a 'remove outliers size=15'. DAPI fluorescence was next segmented with the nuclei outline plugin from GSD. A binary mask and a three-dimensional watershed were finally generated to separate nucleus clusters (Otsu, 1979). An astrocyte nucleus was selected on the basis of its high GFAP immunofluorescence intensity, and was displayed in green. All other detected nuclei were displayed in red. A dialogue box enabled the user to confirm or correct the software's choice of nuclei.
5. The GFAP immunofluorescence was processed using a 0.5 median filter and a binary mask, using Li's threshold method (Li and Lee, 1993). The three-dimensional local thickness of the processes was used to generate a distance map and calculate the local process diameters.
6. For FISH dot channel processing, a value of 500 (a manual estimation of the background after deconvolution) was subtracted from each voxel. A difference of Gaussian filter (kernel: 3–1) and a binary mask were applied, using the threshold method defined in the "parameters"

dialogue box. The mean dot size volume was computed after the exclusion of dot clusters (volume >2 µm^3). For dot clusters (which arise when mRNAs are strongly expressed), the dot number was calculated by dividing the cluster by the previously determined mean dot size volume. For each dot, the mean intensity in the GFAP immunofluorescence channel and the distance map value (the process diameter) was calculated.

7. FISH dots were classified into one of three categories: (a) Dot 0 (in red) was a dot in the immunofluorescence background (without using the 'Specific mRNA' option only): mean GFAP immunofluorescence intensity ≤bgThreshold; distance to the boundary of the nucleus >2 µm. (b) Dot 1 (in yellow) was a dot in a fine process: mean GFAP immunofluorescence intensity >bgThreshold; distance to the boundary of the nucleus >2 µm; astrocyte process diameter <step in the z calibration (0.3 µm). (c) Dot 2 (green) was a dot in a large process: mean GFAP immunofluorescence intensity >bgThreshold; distance to the boundary of the nucleus >2 µm; astrocyte process diameter >step in the z calibration (0.3 µm); or a dot in the soma if the distance to the boundary of the nucleus ≤2 µm. Hence, Dots 1 and 2 were inside astrocytes, and Dots 0 were outside astrocytes.
8. For each image and for each computed ROI, a .csv output table was generated with the following headers: Image name; ROI name; Background intensity; Astrocyte volume; Dot density inside astrocytes (number of dots 1+number of dots 2)/astrocyte volume); Percentage of dots outside the astrocyte (number of dots 0/total dot number); Percentage of dots in astrocyte somata (number of dots less than 2 µm from the boundary of the nucleus/number of dots in astrocytes); Percentage of dots in fine processes (number of dots 1/number of dots in astrocytes); Percentage of dots in large processes [(number of dots 2–number of dots in somata)/number of astrocyte dots]; Mean astrocyte diameter. For each image and each ROI, the selected nucleus, astrocyte channel and classified dot populations were saved as .TIF images.

Astrostat

AstroStat was designed to: (i) define the template analysis using a checkbox (working directory, conditions to be compared, paired or unpaired analysis, or data normality plot); (ii) pool data appropriately for each mouse; (iii) test the normality of the data distribution of each group (using Shapiro's test). If there were more than 30 cells in each group, the central limit theorem was applied; (iv) test the equality of variances (using Fisher's test) for an unpaired analysis; and (v) compare the means using an unpaired or paired analysis. Student's *t*-test was used for normally distributed data and equal variances; Welch-Satterthwaite's test for a normal data distribution and unequal variances; Wilcoxon's test for non-normally distributed data; for paired analyses, a paired Student's *t*-test was used for normally distributed data; Wilcoxon signed rank test for non-normally distributed data. The threshold for statistical significance was set to $P<0.05$.

Acknowledgements

We thank Carole Escartin for the gift of APPswe/PS1dE9 mouse brain slices, and all members of the Orion imaging facility for their high-quality technical support.

Competing interests

The authors declare no competing or financial interests.

Author contributions

Conceptualization: M.O., R.T., P.M., M.C.-S.; Methodology: M.O., R.T., P.M., M.C.-S.; Software: M.O., R.T., P.M.; Validation: M.O., R.T., P.M., N.M., A.-C.B., M.C.-S.; Formal analysis: M.O., R.T., P.M., M.C.-S.; Investigation: M.O., R.T., P.M., N.M., A.-C.B., M.C.-S.; Resources: M.C.-S.; Data curation: M.C.-S.; Writing - original draft: M.C.-S.; Writing - review & editing: M.O., M.C.-S.; Visualization: M.O., M.C.-S.; Supervision: M.C.-S.; Project administration: M.C.-S.; Funding acquisition: M.C.-S.

Funding

This work was funded by the Fondation pour la Recherche Médicale (AJE20171039094; FDT201904008077 to N.M.). R.T. received a grant from the Journées de Neurologie de Langue Francaise. The creation of the Center for Interdisciplinary Research in Biology (CIRB) was funded by the Fondation Bettencourt Schueller.

Supplementary information

Supplementary information available online at
http://jcs.biologists.org/lookup/doi/10.1242/jcs.239756.supplemental

Peer review history

The peer review history is available online at
https://jcs.biologists.org/lookup/doi/10.1242/jcs.239756.reviewer-comments.pdf

References

Alvarez, J. I., Katayama, T. and Prat, A. (2013). Glial influence on the blood brain barrier. *Glia* **61**, 1939-1958. doi:10.1002/glia.22575

Aspelund, A., Antila, S., Proulx, S. T., Karlsen, T. V., Karaman, S., Detmar, M., Wiig, H. and Alitalo, K. (2015). A dural lymphatic vascular system that drains brain interstitial fluid and macromolecules. *J. Exp. Med.* **212**, 991-999. doi:10.1084/jem.20142290

Ben Haim, L., Carrillo-de Sauvage, M. A., Ceyzériat, K. and Escartin, C. (2015). Elusive roles for reactive astrocytes in neurodegenerative diseases. *Front. Cell. Neurosci.* **9**, 278. doi:10.3389/fncel.2015.00278

Borchelt, D. R., Ratovitski, T., van Lare, J., Lee, M. K., Gonzales, V., Jenkins, N. A., Copeland, N. G., Price, D. L. and Sisodia, S. S. (1997). Accelerated amyloid deposition in the brains of transgenic mice coexpressing mutant presenilin 1 and amyloid precursor proteins. *Neuron* **19**, 939-945. doi:10.1016/S0896-6273(00)80974-5

Boulay, A. C., Cisternino, S. and Cohen-Salmon, M. (2016). Immunoregulation at the gliovascular unit in the healthy brain: a focus on Connexin 43. *Brain Behav. Immun.* **56**, 1-9. doi:10.1016/j.bbi.2015.11.017

Boulay, A.-C., Saubaméa, B., Adam, N., Chasseigneaux, S., Mazaré, N., Gilbert, A., Bahin, M., Bastianelli, L., Blugeon, C., Perrin, S. et al. (2017). Translation in astrocyte distal processes sets molecular heterogeneity at the gliovascular interface. *Cell Discov.* **3**, 17005. doi:10.1038/celldisc.2017.5

Boulay, A.-C., Mazare, N., Saubaméa, B. and Cohen-Salmon, M. (2019). Preparing the astrocyte perivascular endfeet transcriptome to investigate astrocyte molecular regulations at the brain–vascular interface. *Methods Mol. Biol.* **1938**, 105-116. doi:10.1007/978-1-4939-9068-9_8

Brehar, F. M., Arsene, D., Brinduse, L. A. and Gorgan, M. R. (2015). Immunohistochemical analysis of GFAP-delta and nestin in cerebral astrocytomas. *Brain Tumor Pathol.* **32**, 90-98. doi:10.1007/s10014-014-0199-8

Burda, J. E. and Sofroniew, M. V. (2014). Reactive gliosis and the multicellular response to CNS damage and disease. *Neuron* **81**, 229-248. doi:10.1016/j.neuron.2013.12.034

Bushong, E. A., Martone, M. E., Jones, Y. Z. and Ellisman, M. H. (2002). Protoplasmic astrocytes in CA1 stratum radiatum occupy separate anatomical domains. *J. Neurosci.* **22**, 183-192. doi:10.1523/JNEUROSCI.22-01-00183.2002

Carney, K. E., Milanese, M., van Nierop, P., Li, K. W., Oliet, S. H., Smit, A. B., Bonanno, G. and Verheijen, M. H. (2014). Proteomic analysis of gliosomes from mouse brain: identification and investigation of glial membrane proteins. *J. Proteome Res.* **13**, 5918-5927. doi:10.1021/pr500829z

Challa, A. A. and Stefanovic, B. (2011). A novel role of vimentin filaments: binding and stabilization of collagen mRNAs. *Mol. Cell. Biol.* **31**, 3773-3789. doi:10.1128/MCB.05263-11

Chever, O., Lee, C. Y. and Rouach, N. (2014). Astroglial connexin43 hemichannels tune Basal excitatory synaptic transmission. *J. Neurosci.* **34**, 11228-11232. doi:10.1523/JNEUROSCI.0015-14.2014

Choi, K. C., Kwak, S. E., Kim, J. E., Sheen, S. H. and Kang, T. C. (2009). Enhanced glial fibrillary acidic protein-delta expression in human astrocytic tumor. *Neurosci. Lett.* **463**, 182-187. doi:10.1016/j.neulet.2009.07.076

Dallérac, G., Zapata, J. and Rouach, N. (2018). Versatile control of synaptic circuits by astrocytes: where, when and how? *Nat. Rev. Neurosci.* **19**, 729-743. doi:10.1038/s41583-018-0080-6

Dossi, E., Vasile, F. and Rouach, N. (2018). Human astrocytes in the diseased brain. *Brain Res. Bull.* **136**, 139-156. doi:10.1016/j.brainresbull.2017.02.001

Heiman, M., Kulicke, R., Fenster, R. J., Greengard, P. and Heintz, N. (2014). Cell type-specific mRNA purification by translating ribosome affinity purification (TRAP). *Nat. Protoc.* **9**, 1282-1291. doi:10.1038/nprot.2014.085

Heo, D. H., Kim, S. H., Yang, K. M., Cho, Y. J., Kim, K. N., Yoon, D. H. and Kang, T. C. (2012). A histopathological diagnostic marker for human spinal astrocytoma: expression of glial fibrillary acidic protein-delta. *J. Neurooncol.* **108**, 45-52. doi:10.1007/s11060-012-0801-z

Hol, E. M. and Pekny, M. (2015). Glial fibrillary acidic protein (GFAP) and the astrocyte intermediate filament system in diseases of the central nervous system. *Curr. Opin. Cell Biol.* **32**, 121-130. doi:10.1016/j.ceb.2015.02.004

Huber, F. M. and Hoelz, A. (2017). Molecular basis for protection of ribosomal protein L4 from cellular degradation. *Nat. Commun.* **8**, 14354. doi:10.1038/ncomms14354

Iadecola, C. (2017). The neurovascular unit coming of age: a journey through neurovascular coupling in health and disease. *Neuron* **96**, 17-42. doi:10.1016/j.neuron.2017.07.030

Kamphuis, W., Mamber, C., Moeton, M., Kooijman, L., Sluijs, J. A., Jansen, A. H. P., Verveer, M., de Groot, L. R., Smith, V. D., Rangarajan, S. et al. (2012).

GFAP isoforms in adult mouse brain with a focus on neurogenic astrocytes and reactive astrogliosis in mouse models of Alzheimer disease. *PLoS ONE* **7**, e42823. doi:10.1371/journal.pone.0042823

Kamphuis, W., Middeldorp, J., Kooijman, L., Sluijs, J. A., Kooi, E. J., Moeton, M., Freriks, M., Mizee, M. R. and Hol, E. M. (2014). Glial fibrillary acidic protein isoform expression in plaque related astrogliosis in Alzheimer's disease. *Neurobiol. Aging* **35**, 492-510. doi:10.1016/j.neurobiolaging.2013.09.035

Li, C. H. and Lee, C. K. (1993). Minimum cross entropy thresholding. *Pattern Recogn.* **26**, 617-625. doi:10.1016/0031-3203(93)90115-D

Li, C. H. and Tam, P. K. S. (1998). An iterative algorithm for minimum cross entropy thresholding. *Pattern Recognit. Lett.* **18**, 771-776.

Liddelow, S. A. and Barres, B. A. (2017). Reactive astrocytes: production, function, and therapeutic potential. *Immunity* **46**, 957-967. doi:10.1016/j.immuni.2017.06.006

Mathiisen, T. M., Lehre, K. P., Danbolt, N. C. and Ottersen, O. P. (2010). The perivascular astroglial sheath provides a complete covering of the brain microvessels: an electron microscopic 3D reconstruction. *Glia* **58**, 1094-1103. doi:10.1002/glia.20990

Middeldorp, J. and Hol, E. M. (2011). GFAP in health and disease. *Prog. Neurobiol.* **93**, 421-443. doi:10.1016/j.pneurobio.2011.01.005

Moeton, M., Stassen, O. M., Sluijs, J. A., van der Meer, V. W., Kluivers, L. J., van Hoorn, H., Schmidt, T., Reits, E. A., van Strien, M. E. and Hol, E. M. (2016). GFAP isoforms control intermediate filament network dynamics, cell morphology, and focal adhesions. *Cell. Mol. Life Sci.* **73**, 4101-4120. doi:10.1007/s00018-016-2239-5

Nolte, C., Matyash, M., Pivneva, T., Schipke, C. G., Ohlemeyer, C., Hanisch, U. K., Kirchhoff, F. and Kettenmann, H. (2001). GFAP promoter-controlled EGFP-expressing transgenic mice: a tool to visualize astrocytes and astrogliosis in living brain tissue. *Glia* **33**, 72-86. doi:10.1002/1098-1136(20010101)33:1<72::AID-GLIA1007>3.0.CO;2-A

Ogata, K. and Kosaka, T. (2002). Structural and quantitative analysis of astrocytes in the mouse hippocampus. *Neuroscience* **113**, 221-233. doi:10.1016/S0306-4522(02)00041-6

Ollion, J., Cochennec, J., Loll, F., Escudé, C. and Boudier, T. (2013). TANGO: a generic tool for high-throughput 3D image analysis for studying nuclear organization. *Bioinformatics* **29**, 1840-1841. doi:10.1093/bioinformatics/btt276

Otsu, N. (1979). A threshold selection method from gray-level histograms. *IEEE Trans. Sys. Man. Cyber* **9**, 62-66. doi:10.1109/TSMC.1979.4310076

Perng, M. D., Wen, S. F., Gibbon, T., Middeldorp, J., Sluijs, J., Hol, E. M. and Quinlan, R. A. (2008). Glial fibrillary acidic protein filaments can tolerate the incorporation of assembly-compromised GFAP-delta, but with consequences for filament organization and alphaB-crystallin association. *Mol. Biol. Cell* **19**, 4521-4533. doi:10.1091/mbc.e08-03-0284

Pilaz, L. J., Lennox, A. L., Rouanet, J. P. and Silver, D. L. (2016). Dynamic mRNA transport and local translation in radial glial progenitors of the developing brain. *Curr. Biol.* **26**, 3383-3392. doi:10.1016/j.cub.2016.10.040

Sakers, K., Lake, A. M., Khazanchi, R., Ouwenga, R., Vasek, M. J., Dani, A. and Dougherty, J. D. (2017). Astrocytes locally translate transcripts in their peripheral processes. *Proc. Natl. Acad. Sci. USA* **114**, E3830-E3838. doi:10.1073/pnas.1617782114

Schindelin, J., Arganda-Carreras, I., Frise, E., Kaynig, V., Longair, M., Pietzsch, T., Preibisch, S., Rueden, C., Saalfeld, S., Schmid, B. et al. (2012). Fiji: an open-source platform for biological-image analysis. *Nat. Methods* **9**, 676-682. doi:10.1038/nmeth.2019

Schmidt, Y., Biniossek, M., Stark, G. B., Finkenzeller, G. and Simunovic, F. (2015). Osteoblastic alkaline phosphatase mRNA is stabilized by binding to vimentin intermediary filaments. *Biol. Chem.* **396**, 253-260. doi:10.1515/hsz-2014-0274

Schneider, C. A., Rasband, W. S. and Eliceiri, K. W. (2012). NIH Image to ImageJ: 25 years of image analysis. *Nat. Methods* **9**, 671-675. doi:10.1038/nmeth.2089

Squarzoni, P., Oller, G., Hoeffel, G., Pont-Lezica, L., Rostaing, P., Low, D., Bessis, A., Ginhoux, F. and Garel, S. (2014). Microglia modulate wiring of the embryonic forebrain. *Cell Rep.* **8**, 1271-1279. doi:10.1016/j.celrep.2014.07.042

Stassen, O., van Bodegraven, E. J., Giuliani, F., Moeton, M., Kanski, R., Sluijs, J. A., van Strien, M. E., Kamphuis, W., Robe, P. A. J. and Hol, E. M. (2017). GFAPdelta/GFAPalpha ratio directs astrocytoma gene expression towards a more malignant profile. *Oncotarget* **8**, 88104-88121. doi:10.18632/oncotarget.21540

Sultan, S., Li, L., Moss, J., Petrelli, F., Cassé, F., Gebara, E., Lopatar, J., Pfrieger, F. W., Bezzi, P., Bischofberger, J. et al. (2015). Synaptic integration of adult-born hippocampal neurons is locally controlled by astrocytes. *Neuron* **88**, 957-972. doi:10.1016/j.neuron.2015.10.037

Thomsen, R., Daugaard, T. F., Holm, I. E. and Nielsen, A. L. (2013). Alternative mRNA splicing from the glial fibrillary acidic protein (GFAP) gene generates isoforms with distinct subcellular mRNA localization patterns in astrocytes. *PLoS ONE* **8**, e72110. doi:10.1371/journal.pone.0072110

van Bodegraven, E. J., van Asperen, J. V., Robe, P. A. J. and Hol, E. M. (2019). Importance of GFAP isoform-specific analyses in astrocytoma. *Glia* **67**, 1417-1433. doi:10.1002/glia.23594

van den Berge, S. A., Middeldorp, J., Zhang, C. E., Curtis, M. A., Leonard, B. W., Mastroeni, D., Voorn, P., van de Berg, W. D., Huitinga, I. and Hol, E. M. (2010). Longterm quiescent cells in the aged human subventricular neurogenic system specifically express GFAP-delta. *Aging Cell* **9**, 313-326. doi:10.1111/j.1474-9726.2010.00556.x

Verkhratsky, A., Nedergaard, M. and Hertz, L. (2015). Why are astrocytes important? *Neurochem. Res.* **40**, 389-401. doi:10.1007/s11064-014-1403-2

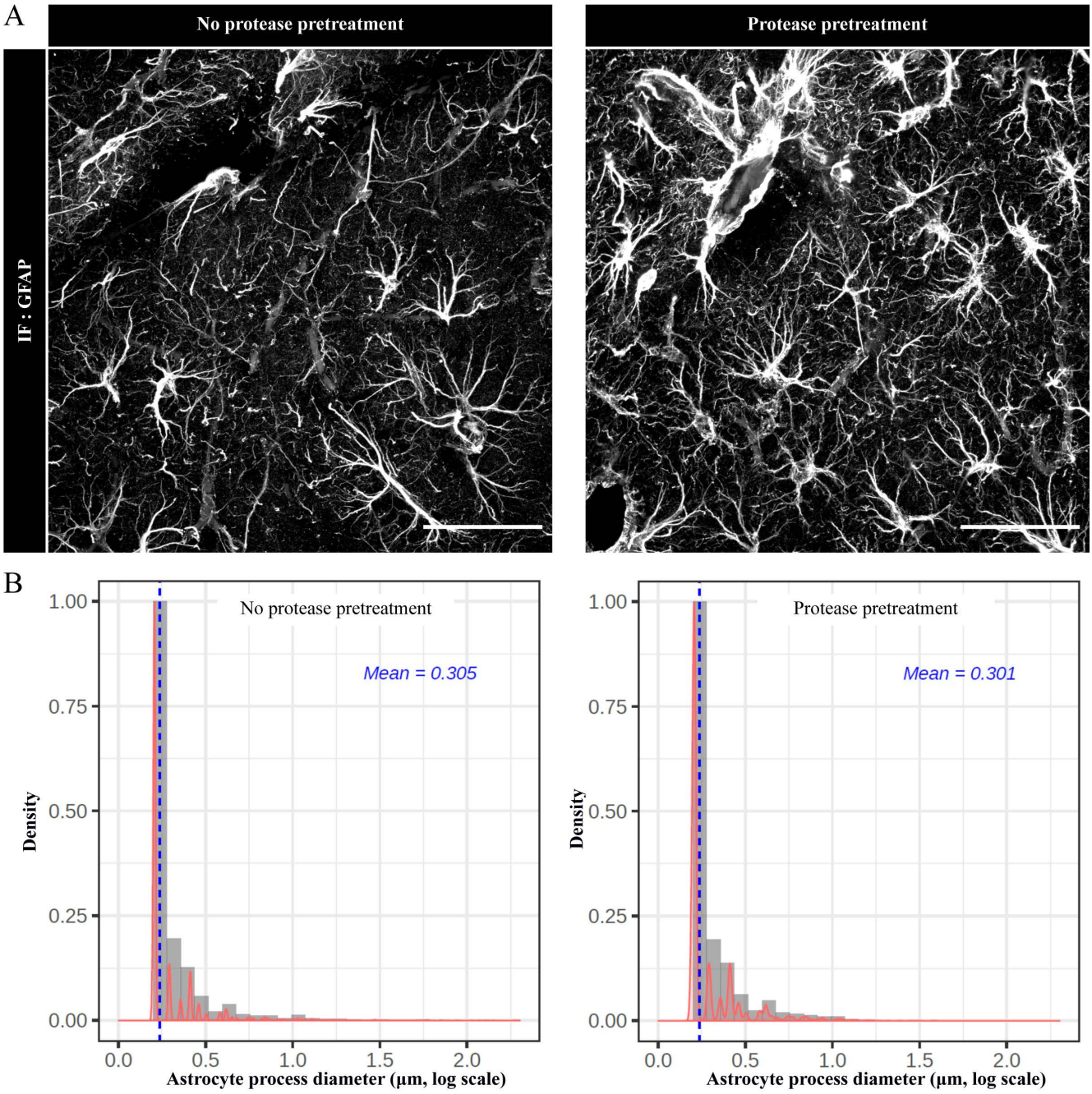

Figure S1: Comparison of GFAP immunolabelling in untreated and protease-treated brain sections. A. Confocal image projections of GFAP immunofluorescent detection in hippocampal sections untreated, or pre-treated with proteases. B. ImageJ analysis of the GFAP-immunolabeled process diameter using the ImageJ plugin *Astro_FineProcess*: For each ROIs, a substack corresponding to the zTop and zBottom was created for all channels. Images were filtered and

thresholded with same parameters as for AstroDot : Astrocyte GFAP channel was processed using a 0.5 median filter size and a binary mask using “Li” threshold method. 3D local thickness calculation was converted into an astrocyte distance map to access the local diameter of astrocyte processes. A skeleton was generated from the binary image mask and for each points, the diameter was extracted from the distance map image. Plots distributions of process diameters were generated in R. The grey bars represent the histograms of the diameter distribution (Gaussian curves in pink). The blue dotted line indicates the mean value of the diameter distribution. 52 astrocytes were analyzed for the untreated condition and 49 for the protease-treated. Scale bars: 50 μm.

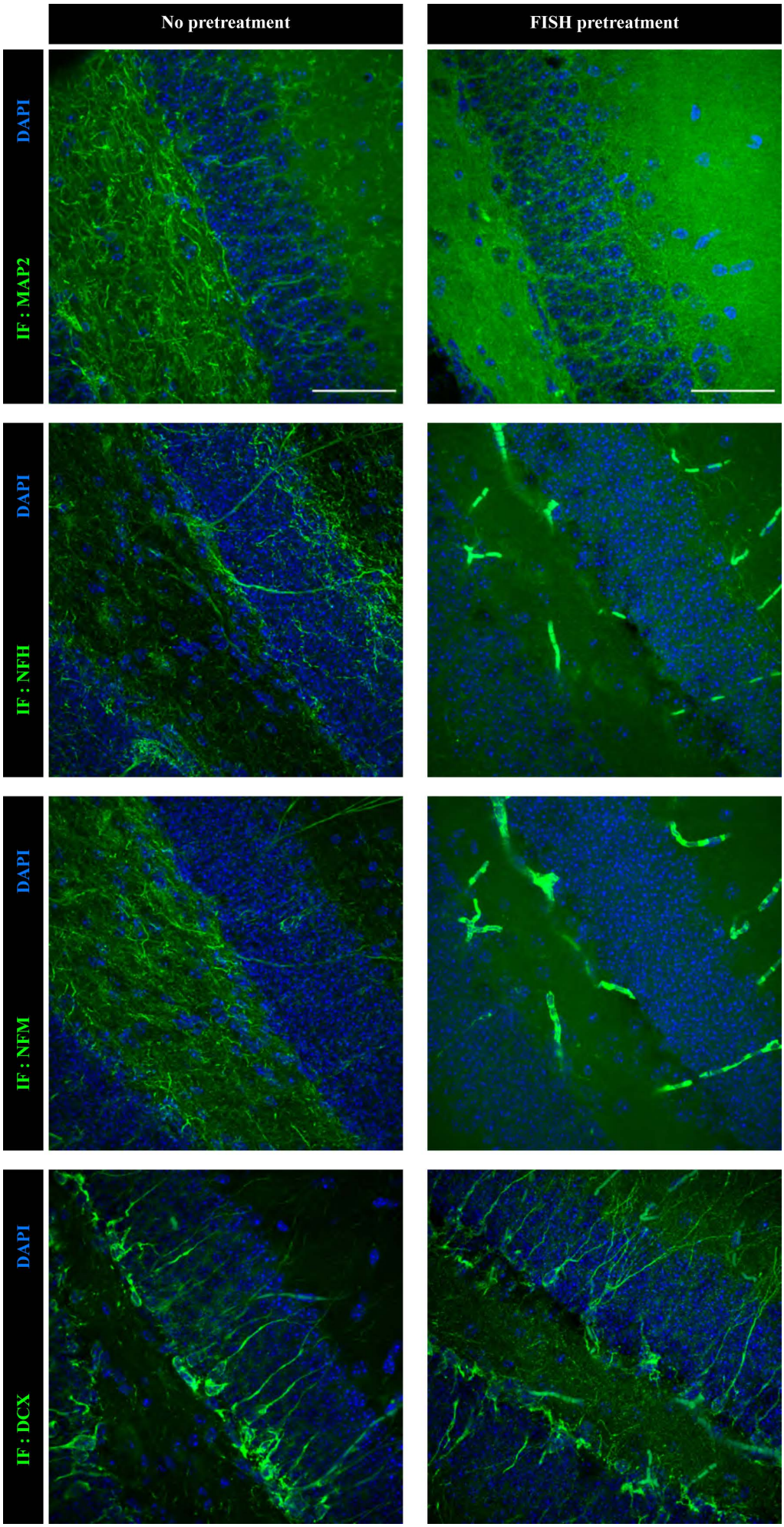
No pretreatment
FISH pretreatment
DAPI
IF : MAP2
DAPI
IF : NFH
DAPI
IF : NFM
DAPI
IF : DCX

Figure S2: Immunolabelling of the neurofilament medium (NF-M) and high (NF-H) chains, the microtubule-associated protein 2 (MAP2) and Doublecortin (DCX) in untreated and protease-treated brain sections. Projection confocal images. NFH and NFM were immunolabeled on the same brain section. In contrast to GFAP and Iba1, the recommended protease treatment used to unmask the mRNAs leads to the degradation of these neuronal epitopes. Scale bars: 50 µm.

Figure S3: FISH target sequences of Gfap α and Gfap δ

Target sequence for GFAP alpha exon 9 probes: Mus musculus glial fibrillary acidic protein (Gfap), transcript variant 2, mRNA NCBI Reference Sequence: NM_010277.3 (copied from emsembl.org)

TCATTAAGGACTCGAAGCAGGAGCACAAGGACGTGGTGATGTGAGGTGTGCCCACCTGG
TGGCCCTTGCCATGCAGTGTGAGGGCCCAAAGCTTATCCTCAAATAGTCCTGTTTGCCAG
GCTCAGTTCCCACCCACACCAGCACTTCCCTTCCTTCTGGTTTTCTGCCTGTGTGCTGCC
CAAGGCTCAATCAGTGCTAAGCTTCATAGATGGCATATACCCTTCACCTTCAACTAACAG
GATACTCACCCCAAAGGCGCAGTCAGGAGGGGAGGGAACCCCAGCTGGGTTAGAATTGGA
AGGGAAGAGGAAAGATGAGCAGAGTAGAGAGATTTAACAAATCACTTCCTTCATCCTTGT
TGTTATGGAAACCGTTGCCAGAGCTGGAAGTTTCCACAGGCTGCTGGAGCTAGACAACAA
TTCAGACAGAAAGGGAAAGTCCCTGAGGCAAAGTCTCTCTAGCCAGAGACCTATGCATCC
CGAATGGCCACTAAGGCAGTCCTGAAGGGCCCTCCAGGGTGATGACTCCAGTGTGTCAGC
CCCACTGAGCAGCTATGCAGGTTGACTGCCCACAGGCATGTGGAAACTTGGTTCTCAGCA
CTTGGCAGGATCTATGGCATAAGTGGAGAGGGAAGGTGTACTGGACGGCGGAGAGGAGGG
CTCCCTGGCCCCTAAGTGTGGATGCAGAGAGGTGGAGCCCAGGAAGGGTCTCTGCTTAGG
CTGCAGGGGTGCCAATGGCAGAGGCACTGGTAGAGATCATTTGGACACTGGAGTTGAAAG
TTACAGGCAATCTGTTACACTTGGCTCTGAATCCTATGAATCAAGGAAATAACCCGTTCT
CTGGAAGACACTGAAACAGGAGAGAGGGACTTCCGTCCACTGGGCAGGGTACAGATGTGT
CTCAGTTGTGAAGGTCTATTCCTGGCTGCACAGTCCCCATCCGCTCAGTCATCTTACCCT
GTGACTGCTCTCAGCCCTGAAGAATCCACAACCATCCTTCCAAGGTTCTCCATCCCCACA
ATGACTAGCTGTTGCTCTCCAAGCTAAGGGACCATTCCCTGTCTTATGCATATACGTAAT
GTCACCTATTTAGGTATCATCCTATTTGAGAGTTTGAGGAACTGAAACGTGTTGTGTTCA
AGCAGCCTGGTGGCTAGTGCCTTCATATTAGAGCACCTTCTCTGAGGCTGATTGGTGGGC
AGGTAGGGAAGACATTGAGCAGACAGTGTCCGCTCAGTTGTCCTTCCCTCCCTTCCAAGG
TCCCTCCCTCTTTCCAGGACATCGCCCCCCACCCCACCCCTCCTTTCCACCTCCGCTAA
CCTCCAGAGCAGTACTGTCACCTTTACTCACTGGGCAGAAATAAAGACATGTGCCATAGA
CTTCCA

Target sequence for GFAP delta exon 8 probes: Mus musculus glial fibrillary acidic protein (Gfap), transcript variant 1, mRNA NCBI Reference Sequence: NM_001131020.1 (copied from emsembl.org)

GGGCAAAAGCACCAAAGAAGGGGAAGGCCAAAAAGTCACAAGACCTCTCAAAAGGCTCA
CAATACAAGTTGTCCCAATACAGGCTCACCAGATTGAAAATGGAGCCCTGCCAGCTCTCC
CTTAGATAGATTGCGTGCTCCAGCTCTCCCTTAGATAGAGGCGTGCTCCAGCTCTCCCTTA
GATAGAGGCGTGCTCCAGCTCTCCCTTAGATAGAGGCGTGCTCCAGCTCTCCCTTAGATA
GAGGCGTGCTCCAGCTCTCCCTTAGATAGAGGCGTGCTCCAGCTCTCCCTTAGATAGATG
CGCGCATTTCAGCCACACCTTTCCAGCTTGTCTTCTTCCTCCCAGGCCTCCTCTAAGGGA
CTGAACCATGTCCTTTGTCTAGAAGCTTCCAGGCCCACCCTAGGTCCTGGCTCTGTGTAA
TTAGGTTATACCGATAGAGCTAGCCTATGCTAAAGGTTAGGTTGTACTAACAGAGCTAGC
CTATGCTAAAGGTTAGGTTGTACTAATAGAGCTAGTCTTATGCTAAAGGTTAGGTTGTATT
TAACAGAGCTAGCCTATGCTAAAGGTTAGGTTGTACTAACAGAGCTAGTCATGTTAAGTT
AGGTTGTACTAACAGAGCTAGCTTATGCTAAAGTTAGGTTGTACTAACATAGCTAGCCTA
TGCTAAAGGTTTGGTTGTACTAACAGAGCTGGCCTATGTTAAAGGTTAGGTTGTACTAAT
AGAGCTAGTCTTATGCTAAAGGTTAGGTTGTATTAACAGAGCTAACCTATGCTAAAGGTT
AGGTTGTACTAACAGAGCTGGCCTATGTTAAAGGTTAGGTTGTACTAATAGAGCTAGCCT
ATGCTAAAGGTTAGGTTGTACTAACAGAGCTGGCCTATGTTAAAGGTTAGGTTTTACTAA
TAGAGCTAGTCTTATGCTAAAGGTTAGGTTGTACTAACAGAGCGAGCCTATGCTAAAGAT
TAGGTTATATTAACAGAGCTAGCCTATGCTAAAGGTTAGGTTGTACTAATAGAGCTAGCC
TATGCTAAAGGTTAGGTTGTACTAATAGAGCTAGCCTATGCTAAAGGTTAGGTTGTATTA
ACAGAGCTAGCCAATGTTAAAGGCAGCAAGTCCCTGGGAGCTCCAAGGAGATACTCTGAA
CCCTCTGAGCAAATGCCTCCGGCTCACCAGTTTCTGTCGCTAGGTGGTCCCCTTGGGTCT
TGCAGTGCCTGTGGGCAGGCTCTGTGTTTGATTCATGTGTCCCCAGAGTTCTATTGCTTC
ACTTCAGTGCTGATTCAGCCCAGAGGGTTAGTTAGTTCCCTCTGGACGGCTGCTCTTGTA
GTGAATAAAGCTTTATGCTCCCTGCTCTTCATTTT

Table S1: Antibodies, qPCR and FISH probes and reagents

qPCR probes		
Gene name	**Supplier**	**Reference**
Gfap α RNA (mouse)	BioRad	10042961 (HEX) dMmuCNS635118061
Gfap δ RNA (mouse)	BioRad	10042958 (FAM) dMmuCNS795284650
Rpl4 RNA (mouse)	ThermoFisher Scientific	4331182 (FAM) Mm00834993_g1
45S RNA (mouse)	ThermoFisher Scientific	4426961 (FAM) Mm03985792_s1

FISH reagents		
Name	**Supplier**	**Reference**
RNAscope® Multiplex Fluorescent detection reagent V2	Advanced Cell Diagnostic	323110
RNAscope® H_2O_2 and Protease	Advanced Cell Diagnostic	322381
Fluoromount-G®	Southern Biotech	0100-01
Coverglass 0.13 – 0.17mm thick	Immuno Cell	65.300.13
SuperFrost® Plus slides	VWR	631-0108
Hydrophobic immunostaining pen	Vector laboratories	H-4000

FISH RNA probes			
Gene name	**Probe**	**Reference and supplier**	**Dilution**
Gfap α RNA	RNAscope® Probe – Mm-Gfap-O2-C2	557051-C2 Advanced Cell Diagnostic	1:1[e]
Gfap δ RNA	RNAscope® Probe – Mm-Gfap-03	557061 Advanced Cell Diagnostic	1:1[e]
Rpl4 RNA	RNAscope® Probe – Mm-Rpl4	535821 Advanced Cell Diagnostic	1:1[e]
FISH Fluorophore			
Name		**Reference and supplier**	**Dilution**
Opal 570		FP14488A Perkin Elmer	1:1500[e]
Opal 650		FP1496A Perkin Elmer	1:1500[e]

Antibodies		
Name	**Reference and supplier**	**Dilution**
Rabbit anti-Glial Fibrillary Acidic Protein (GFAP) antibody	G9269 Sigma	1:500[e]
Rabbit anti-Iba1	W1w019-19741 Sobioda	1:500[e]
Mouse anti-Neurofilament medium polypeptide (NFM)	Given by Dr. Beat M. RIEDERER, University of Lausanne, Switzerland	1:10[e]
Chicken anti-Neurofilament heavy polypeptide (NFH)	Ab4680 Abcam	1:500[e]
Rabbit anti-Doublecortin (DCX)	4604S Cell signaling	1:500[e]
Mouse anti-MAP2	M4403 Sigma-Aldrich	1:500[e]
Goat anti-Rabbit IgG (H+L) Highly Cross-Adsorbed Secondary Antibody, Alexa Fluor 488	A11034 Invitrogen	1:1000[e]
Goat anti-Rabbit IgG (H+L), Superclonal™ Recombinant Secondary Antibody, Alexa Fluor 647	A27040 Invitrogen	1:1000[e]

Table S2: Astrodot and Astrostat raw data for Gfap α and Gfap δ mRNAs in CA1 and CA3 hippocampal astrocytes from WT and APPswe/PS1dE9 mice
SD, standard deviation; N, number of cells analyzed

		Gfap α WT	SD	N	Non-Aβ-associated	SD	N	AB-associated	SD	N
RNA FISH density	*CA1*	1,59	0,7	175	2,11	1,21	127	8,06	4,66	27
	CA3	1,77	0,75	94	2,25	1,3	78	8,42	5,07	28
% RNA in the soma	*CA1*	11,49	6,77	175	10,16	4,91	127	7,96	4,6	27
	CA3	13,27	8,15	94	9,56	5,12	78	7,1	3,69	28
% RNA in large processes	*CA1*	12,44	4,42	175	11,79	4,54	127	9,61	2,88	27
	CA3	12,29	4,91	94	10,8	4,19	78	11,6	4,09	28
% RNA in fine processes	*CA1*	76,07	7,56	175	78,05	6,46	127	82,43	5,85	27
	CA3	74,45	7,61	94	79,64	7,04	78	81,3	5,6	28
% RNA in GFAP+ processes	*CA1*	59,48	9,04	175	59,29	7,8	127	60,07	7,71	27
	CA3	62,16	10,05	94	56,38	6,52	78	59,35	8,29	28
		Gfap δ WT	**SD**	**N**	**Non-Aβ-associated**	**SD**	**N**	**AB-associated**	**SD**	**N**
RNA FISH density	*CA1*	0,33	0,17	175	0,36	0,18	127	1,16	0,76	27
	CA3	0,35	0,17	94	0,36	0,18	78	1,24	0,77	28
% RNA in the soma	*CA1*	26,51	13,52	175	26,81	11,38	127	26,98	9,66	27
	CA3	28,5	16,39	94	25,2	12,1	78	24,85	14,09	28
% RNA in large processes	*CA1*	19,54	9,19	175	17,4	7,73	127	14,08	5,73	27
	CA3	17,64	9	94	14,79	6,84	78	13,81	4,73	28
% RNA in fine processes	*CA1*	53,95	14,67	175	55,79	11,21	127	58,94	9,47	27
	CA3	53,86	15,74	94	60,02	10,64	78	61,34	14,5	28
% RNA in GFAP+ processes	*CA1*	74,41	11	175	73,91	7,73	127	75,63	7,57	27
	CA3	74,66	12,41	94	69,01	8,43	78	73,66	8,75	28
		WT	**SD**	**N**	**Non-Aβ-associated**	**SD**	**N**	**AB-associated**	**SD**	**N**
Astrocyte volume (µm^3)	*CA1*	11541,3	4277,5	175	18264,9	6355	127	19550,01	8747,7	27
	CA3	10430,5	3842,5	94	18181,5	5395	78	15144,21	6640,6	28
Astrocyte process diameter (mean, in µm)	*CA1*	0,32	0,03	175	0,3	0,02	127	0,26	0,02	27
	CA3	0,32	0,04	94	0,29	0,02	78	0,29	0,02	28
Gfap α/ Gfap δ RNA	*CA1*	5,22	1,7	175	6,02	1,62	127	7,29	1,48	27
	CA3	5,25	1,42	94	6,13	1,38	78	7,14	2,19	28

Table S3: Comparison of AstroDot data for Gfap α and Gfap δ mRNAs between CA1 and CA3 hippocampal astrocytes in WT and APPswe/PS1dE9

SD, standard deviation; N, number of cells analyzed

CA1 versus CA3

		WT	Non-Aβ-associated	AB-associated
Astrocyte volume (µm³)	***Fold Change***	1,11	1,00	1,29
	p-value	3.57E-02 (*)	9.23E-01 (NS)	6.01E-02 (NS)
Mean astrocyte process diameter (µm)	***Fold Change***	1,00	1,03	0,90
	p-value	3.91E-01 (NS)	2.61E-02 (*)	5.87E-01 (NS)
Ratio Gfap α/ Gfap δ RNA	***Fold Change***	0,99	0,98	1,02
	p-value	9.08E-01 (NS)	6.27E-01 (NS)	7.67E-01 (NS)

		Gfap α			Gfap δ		
		WT	**Non-Aβ-associated**	**AB-associated**	**WT**	**AB-not associated**	**AB-associated**
RNA FISH density	***Fold Change***	0,90	0,94	0,96	0,94	1,00	0,94
	p-value	5.26E-02 (NS)	4.55E-01 (NS)	8.61E-01 (NS)	2.21E-01 (NS)	7.49E-01 (NS)	6.46E-01 (NS)
% RNA in the soma	***Fold Change***	0,87	1,06	1,12	0,93	1,06	1,09
	p-value	7.15E-02 (NS)	4.05E-01 (NS)	5.99E-01 (NS)	3.16E-01 (NS)	3.37E-01 (NS)	5.18E-01 (NS)
% RNA in large processes	***Fold Change***	1,01	1,09	0,83	1,11	1,18	1,02
	p-value	7.95E-01 (NS)	1.21E-01 (NS)	1.12E-01 (NS)	1.04E-01 (NS)	1.50E-02 (*)	1.00E00 (NS)
% RNA in fine processes	***Fold Change***	1,02	0,98	1,01	1,00	0,93	0,96
	p-value	9.36E-02 (NS)	1.01E-01 (NS)	4.67E-01 (NS)	9.65E-01 (NS)	8.13E-03 (**)	4.70E-01 (NS)
% RNA in GFAP+ processes	***Fold Change***	0,96	1,05	1,01	1,00	1,07	1,03
	p-value	2.60E-02 (*)	6.36E-03 (**)	7.39E-01 (NS)	8.67E-01 (NS)	3.20E-05 (****)	2.89E-01 (NS)

Table S4: Comparison of AstroDot data for Gfap α and Gfap δ mRNAs between WT and APPswe/PS1dE9 hippocampal astrocytes

SD, standard deviation; N, number of cells analyzed

APP/PS1dE9 versus WT				
			Not-Aβ-associated / WT	Aβ-associated / WT
Astrocyte volume (µm^3)	CA1	*Fold Change*	1,58	1,69
		p-value	1.80E-20 (****)	3.91E-06 (****)
	CA3	*Fold Change*	1,74	1,45
		p-value	1.22E-19 (****)	7.95E-06 (****)
Astrocyte process diameter (mean, in µm)	CA1	*Fold Change*	0,94	0,81
		p-value	3.16E-13 (****)	3.23E-08 (****)
	CA3	*Fold Change*	0,91	0,91
		p-value	3.21E-08 (****)	1.04E-04 (***)
Gfap α/ Gfap δ RNA	CA1	*Fold Change*	1,15	1,40
		p-value	5.05E-05 (****)	2.05E-08 (****)
	CA3	*Fold Change*	1,17	1,36
		p-value	6.12E-05 (****)	1.34E-04 (***)

			Gfap α		Gfap δ	
			Not-Aβ-associated / WT	Aβ-associated / WT	Not-Aβ-associated/ WT	Aβ-associated / WT
RNA FISH density	CA1	*Fold Change*	1,33	5,07	1,09	3,52
		p-value	2.27E-05 (****)	3.66E-16 (****)	1.50E-01 (NS)	8.00E-14 (****)
	CA3	*Fold Change*	1,27	4,76	1,03	3,54
		p-value	4.81E-03 (**)	3.77E-12 (****)	6.85E-01 (NS)	7.94E-10 (****)
% RNA in the soma	CA1	*Fold Change*	0,88	0,69	1,01	1,02
		p-value	4.93E-02 (*)	3.86E-03 (**)	8.35E-01 (NS)	8.27E-01 (NS)
	CA3	*Fold Change*	0,72	0,54	0,88	0,87
		p-value	3.67E-04 (***)	5.53E-05 (****)	1.31E-01 (NS)	3.99E-01 (NS)
% RNA in large processes	CA1	*Fold Change*	0,95	0,77	0,89	0,72
		p-value	2.10E-01 (NS)	9.07E-04 (***)	2.92E-02 (*)	1.34E-03 (**)
	CA3	*Fold Change*	0,88	0,94	0,84	0,78
		p-value	3.53E-02 (*)	4.42E-01 (NS)	1.95E-02 (*)	1.71E-02 (*)
% RNA in fine processes	CA1	*Fold Change*	1,03	1,08	1,03	1,09
		p-value	1.76E-02 (*)	1.27E-05 (****)	2.18E-01 (NS)	2.83E-02 (*)
	CA3	*Fold Change*	1,07	1,09	1,11	1,14
		p-value	7.53E-06 (****)	1.24E-05 (****)	2.73E-03 (**)	2.67E-02 (*)
% RNA in GFAP+ processes	CA1	*Fold Change*	1,00	1,01	0,99	1,02
		p-value	8.54E-01 (NS)	7.46E-01 (NS)	6.42E-01 (NS)	5.16E-01 (NS)
	CA3	*Fold Change*	0,91	0,95	0,92	0,99
		p-value	1.02E-05 (****)	1.80E-01 (NS)	5.30E-04 (***)	4.30E-01 (NS)

Table S5: Number of astrocytes analyzed per mouse and hippocampal regions

Number of astrocytes per mice				
Brain region	**Genotype**	**Mice identification number**	**Number of astrocytes analyzed**	**Total**
CA1	WT	009	51	
		013	70	
		017	54	175
CA3	WT	009	29	
		013	29	
		017	36	94
CA1	APPswe/PS1dE9 / not-Aβ associated	008	56	
		010	38	
		014	33	127
CA3	APPswe/PS1dE9 / not-Aβ associated	008	33	
		010	14	
		014	31	78
CA1	APPswe/PS1dE9/ Aβ associated	008	11	
		010	5	
		014	11	27
CA3	APPswe/PS1dE9/ Aβ associated	008	7	
		010	5	
		014	16	28